Comparison of Dynamic Characteristics of Virtual Synchronous Machine Control Algorithms

by

Theja Thilekha Muthukumarana Hewa Thondilege

A Thesis submitted to the Faculty of Graduate Studies of The

University of Manitoba

in partial fulfilment of the requirements of the degree of

MASTER OF SCIENCE

Department of Electrical and Computer Engineering

University of Manitoba

Winnipeg

Abstract

Renewable energy sources and energy storage systems will hold increasingly significant positions in modern power systems. These systems utilize power-electronic converters as the medium for connection to the grid. The decoupling of the generation and the grid frequency support is a main drawback of conventional converter control topologies. The concept of a *virtual synchronous machine* (VSM) has gained attention to address this issue in numerous topologies. This thesis provides a detailed insight into several recently proposed VSM algorithms. A VSM categorization is introduced, which can be generally applied to any VSM topology. EMT simulations in PSCAD/EMTDC are carried out to show the performance of the selected key VSM algorithms for large-signal disturbances. The selected VSM algorithms are tested explicitly for grid-forming functionality. Their performances are compared against the conventional synchronous machine. The results show the impact of controller parameters on VSM's performance and possible ways of improvements.

Acknowledgements

This thesis has become a success with the support given by many amazing individuals at the University of Manitoba and Transgrid Solutions (TGS).

First and foremost, I would like to thank my advisor, Prof. Shaahin Filizadeh, for his guidance, support, and invaluable encouragement given throughout the research. I would also like to thank my co-advisor, Prof. Udaya Annakkage, for the support and guidance given to complete the research.

I extend my sincere gratitude to Dr. Chandana Karawita from TGS for the knowledge sharing and the attention given to every detail of my research. The insights given by many industrial expertise at TGS helped me to investigate the issues in a broader mindset.

I would like to thank Mr. Shrimal Koruwage for handling technical issues related to the software packages, especially during the time when I had to work remotely.

I thank my family and friends for their support and encouragement during my M.Sc.

Last but not least, I would like to thank TGS, MITACS, and the Natural Sciences and Engineering Research Council (NSERC) of Canada for providing financial support to carry out my research.

Dedication

To my parents.

Contents

Chapter 1 : Introduction 1
1.1 Background 1
1.2 Problem Definition 6
1.3 Thesis Motivation 6
1.4 Organization of the Thesis 7
Chapter 2 : VSM Topologies 8
2.1 Overview of VSM Topologies 8
2.1.1 Droop-based model 8
2.1.2 Swing equation-based model 10
2.1.3 Full model 13
2.1.4 Simplified model 14
2.2 A Comparison between a SM and a VSM 14
Chapter 3 : Major VSM Algorithms 18
3.1 VSM0H Model 18
3.2 VC-VSC Model 20
3.3 Modified-VSM0H Model 22
3.4 Synchronverter Model 24
Chapter 4 : Detailed Assessment 28
4.1 Study System 28
4.1.1 Inverter 29
4.1.2 LCL filter 30
4.2 SM Time-Domain Simulation Results 32
4.3 VSM0H Time-Domain Simulation Results 39
4.4 VC-VSC Time-Domain Simulation Results 47
4.5 Modified-VSM0H Time-Domain Simulation Results 51
4.6 Synchronverter Time-Domain Simulation Results 54
Chapter 5 : Contributions, Conclusions and Recommendations for Future Work 59
5.1 Contributions 59
5.2 Conclusions 59

5.3 Future Work 60
References 61

List of Tables

Table 4.1 Parameters of the study system 28
Table 4.2 Parameters of the short transmission line 28
Table 4.3 The SM parameters 33
Table 4.4 AC1A Exciter parameters 33
Table 4.5 Hydro turbine parameters 33
Table 4.6 Hydro governor parameters 34
Table 4.7 VSM0H controller parameters 40
Table 4.8 VC-VSC controller parameters 47
Table 4.9 Modified VSM0H controller parameters 51
Table 4.10 Synchronverter controller parameters 55

List of Figures

Figure 1.1 Typical frequency response of a power system following a generator tripping..... 2
Figure 1.2 Vector control algorithm 3
Figure 1.3 The rotor of a SM with a moment of inertia of J and nominal mechanical speed of ω_{0m} 4
Figure 1.4 A capacitor with capacitance of C_{dc} and nominal voltage of V_{dc} 4
Figure 2.1 The arrangement of the considered system 8
Figure 2.2 Droop-based controller without voltage and current controllers..... 9
Figure 2.3 Droop based controller with voltage and current limiters 10
Figure 2.4 The phase angle calculation based on swing-equation..... 11
Figure 2.5 EMF magnitude calculation based on (a) *Q*-controller (b) *V*-Controller 11
Figure 2.6 Swing equation based cascaded controller 12
Figure 2.7 VISMA concept..... 13
Figure 2.8 The comparison of grid forming capability of a (a) VSM, (b) SM 14
Figure 3.1 VSM0H model..... 19
Figure 3.2 Frequency droop control block..... 19
Figure 3.3 VC-VSC model (a) *P-f* controller, (b) *Q-v* controller. 21
Figure 3.4 The modified VSM0H model (a) *P-f* controller, (b) *Q-v* controller. 23
Figure 3.5 An idealized two-pole, round rotor SG representation. 24
Figure 3.6 The synchronverter model 26
Figure 3.7 Self-synchronizing synchronverter..... 27
Figure 4.1 Single-line diagram of the study system 28
Figure 4.2 (a) The SPWM generator (b) Two-level VSC arrangement..... 30
Figure 4.3 The single-line diagram of the LCL filter connecting VSC and the grid. 30
Figure 4.4 The effect of damping resistor on the LCL filter performance 32
Figure 4.5 SM's (a) active power supply at PCC, (b) reactive power supply at PCC, (c) governor valve position, (d) rotor speed, (e) external frequency from PLL, (f) mechanical torque variation following the 0.1 pu constant P load addition..... 35
Figure 4.6 SM's (a) active power output, (b), reactive power output, (c) load current, (d) terminal voltage, (e) voltage at PCC, (f) field voltage variation for the 0.1 pu constant L load addition .. 36
Figure 4.7 SM's (a) active power at terminal, (b) reactive power at terminal, (c) terminal voltage, (d) load current, (e) active power at PCC, (f) reactive power at PCC, (g) voltage at PCC, (h) field voltage variation for solid three phase-ground fault at PCC for 0.1 s 38
Figure 4.8 The rotational speed variation for a solid three phase-ground fault at PCC for 0.1 s 39
Figure 4.9 SM's (a) active power at terminal, (b) reactive power at terminal, (c) terminal voltage, (d) load current (e) active power at PCC, (f) reactive power at PCC, (g) volatage at PCC, (h) rotational speed variation for HIF three phase-ground fault at PCC for 0.1 s 40
Figure 4.10 VSM0H model's (a) active power at PCC, (b) reactive power at PCC, (c) virtual rotor speed, (d) system frequency (PLL), (e) dc power variation following the 0.1 pu constant P load addition..... 42

Figure 4.11 VSM0H model's (a) active power at PCC, (b) reactive power at PCC, (c) VSM terminal voltage, (d) voltage at PCC, (e) modulation index variation following the 0.1 pu of constant L load addition 42
Figure 4.12 The impact on frequency nadir from different low pass filter band widths 43
Figure 4.13 VSM0H model's (a) active power at VSM terminal, (b) reactive power at VSM terminal, (c) VSM terminal voltage, (d) VSM virtual rotor speed, (e) active power at PCC, (f) reactive power at PCC, (g) volatage at PCC, (h) load current variation for solid three phase-ground fault at PCC for 0.1 s 45
Figure 4.14 VSM0H model's (a) active power at VSM terminal, (b) reactive power at VSM terminal, (c) VSM terminal voltage, (d) VSM virtual rotor speed, (e) active power at PCC, (f) reactive power at PCC, (g) voltage at PCC, (h) load current variation for high impedance three phase-ground fault at PCC for 0.1 s 46
Figure 4.15 VC-VSC model's (a) active power at PCC, (b) reactive power at PCC, (c) virtual rotor speed, (d) system frequency (PLL), (e) dc power variation following the 0.1 pu constant P load addition 48
Figure 4.16 VC-VSC model's (a) active power at PCC, (b) reactive power at PCC, (c) VSM terminal voltage, (d) voltage at PCC, (e) modulation index variation following the 0.1 pu of constant L load addition 48
Figure 4.17 Impact of inertia time constant in frequency response 48
Figure 4.18 VC-VSC model's (a) active power at VSM terminal, (b) reactive power at VSM terminal, (c) VSM terminal voltage, (d) VSM virtual rotor speed, (e) active power at PCC (f) reactive power at PCC, (g) volatage at PCC, (h) load current variation for solid three phase-ground fault at PCC for 0.1 s 49
Figure 4.19 VC-VSC model's (a) active power at VSM terminal, (b) reactive power at VSM terminal, (c) VSM terminal voltage, (d) VSM virtual rotor speed, (e) active power at PCC, (f) reactive power at PCC, (g) voltage at PCC, (h) load current variation for high impedance three phase-ground fault at PCC for 0.1 s 50
Figure 4.20 Modified VSM0H model's (a) active power at PCC, (b) reactive power at PCC, (c) virtual rotor speed, (d) system frequency (PLL), (e) dc power variation following the 0.1 pu constant P load addition 52
Figure 4.21 Modified VSM0H model's (a) active power at PCC, (b) reactive power at PCC, (c) VSM terminal voltage, (d) voltage at PCC, (e) modulation index variation following the 0.1 pu of constant L load addition 52
Figure 4.22 Impact of different inertia time constants, damping co-efficient and integral time constant of the PI controller on the frequency response. 53
Figure 4.23 Modified VSM0H model's (a) active power at VSM terminal, (b) reactive power at VSM terminal, (c) VSM terminal voltage, (d) VSM virtual rotor speed, (e) active power at PCC (f) reactive power at PCC, (g) volatage at PCC, (h) load current variation for solid three phase-ground fault at PCC for 0.1 s 54
Figure 4.24 Modified VSM0H model's (a) active power at VSM terminal, (b) reactive power at VSM terminal, (c) VSM terminal voltage, (d) VSM virtual rotor speed, (e) active power at PCC, (f) reactive power at PCC, (g) voltage at PCC, (h) load current variation for high impedance three phase-ground fault at PCC for 0.1 s 55

Figure 4.25 Synchronverter model's (a) active power at PCC, (b) reactive power at PCC, (c) virtual rotor speed, (d) system frequency (PLL), (e) dc power variation following the 0.1 pu constant P load addition 56
Figure 4.26 Synchronverter model's (a) active power at PCC, (b) reactive power at PCC, (c) VSM terminal voltage, (d) voltage at PCC, (e) modulation index variation following the 0.1 pu of constant L load addition 56
Figure 4.27 Synchronverter model's (a) active power at VSM terminal, (b) reactive power at VSM terminal, (c) VSM terminal voltage, (d) VSM virtual rotor speed, (e) active power at PCC, (f) reactive power at PCC, (g) voltage at PCC, (h) load current variation for a three phase-ground soild fault at PCC for 0.1 s 57
Figure 4.28 Synchronverter model's (a) active power at VSM terminal, (b) reactive power at VSM terminal, (c) VSM terminal voltage, (d) VSM virtual rotor speed, (e) active power at PCC, (f) reactive power at PCC, (g) voltage at PCC, (h) load current variation for three pahse-ground high impedance fault at PCC for 0.1 s 58

List of Abbreviations

RES	renewable energy sources
PV	photovoltaic
SG	synchronous generators
LED	light emitting diode
PHEV	plug-in hybrid electric vehicles
PI	proportional integral
dq0	direct-quadrature-zero
DFIGs	doubly fed induction generators
PMSGs	permanent magnet synchronous generators
ESS	energy storage systems
BESS	battery energy storage systems
VSM	virtual synchronous machines
PWM	pulse-width modulation
P-f	active power-frequency
Q-v	reactive power-voltage
PCC	point of common coupling
emf	electromotive force
SOC	state of charge
VSM0H	virtual synchronous machine zero inertia
VC-VSC	voltage controller voltage source converter
EMT	electromagnetic transients

Chapter 1 : Introduction

1.1 Background

Renewable energy sources (RES) are growing faster than any other energy sources in the global energy context. In 2018, 26.2% of the worldwide electricity generation was produced by RES, with an expected increase to 45% in 2040 [1]. Sharp decline in the capital cost of photovoltaic (PV) and wind power generation, faster installation, interconnection and commissioning ability, modularity, large-scale digitalization, and government incentives together with favorable energy policies have accelerated the RES integration [2], [3]. The power system of the future will include a larger number of small-scale, distributed, converter-tied power plants than conventional, large, centralized synchronous generators (SGs). Conventional loads will also be outnumbered by converter-interfaced ones. Plug-in hybrid electric vehicles (PHEVs), light emitting diodes (LEDs), motor drives to connect various electric motors to the grid, computer-intensive appliances, and other forms of power electronic systems will be connected via converters. This will pave the way for unified control of generators and loads connected via converters [4].

Proliferation of RES has already caused a number of issues in the operation and control of power systems. The intermittent nature of RES results in lower dispatchability and increases the spinning reserve requirement. The situation is exacerbated by the frequent start-up and shutdown of large SGs. The distribution network is also facing major challenges due to industrial- and domestic-scale PV panel interconnections, PHEVs, and other convert-tied loads. This has the potential to overwhelm the existing distribution network [3]. Further, the presence of converters will increase the current and voltage harmonics resulting in degraded power quality [3].

Converter-tied generation has also threatened the stability of power systems by replacing large rotating masses of conventional generators with new forms of generation with no or negligible inertia. The frequency dictates the generation and load balance in the power system. The inertia of a power system measures the reluctance of system frequency variations to generation-load imbalances. As converters effectively decouple the source from the grid, larger levels of converter-coupled generation result in less inertial support, which will in turn deteriorate the system frequency’s nadir [5]. Figure 1.1 shows a typical frequency variation following a generator tripping.

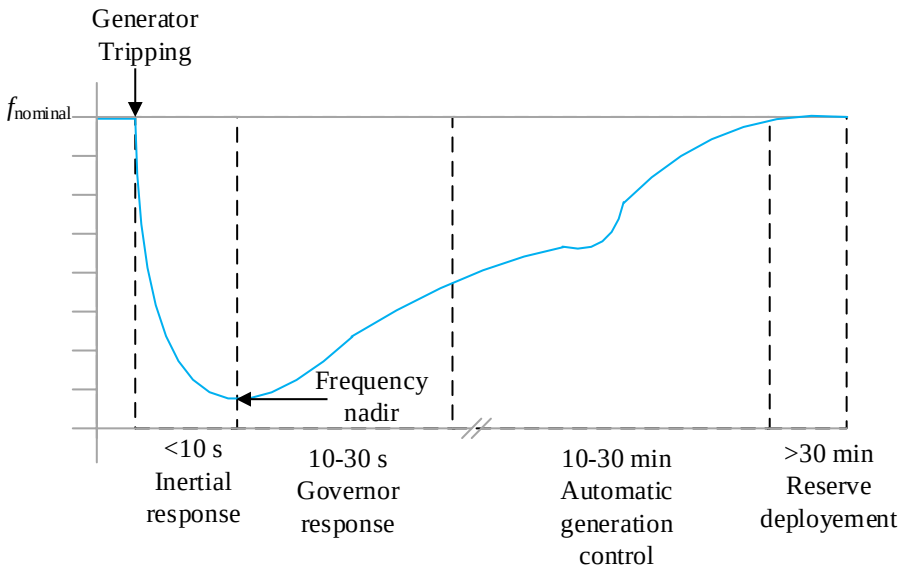

Figure 1.1 Typical frequency response of a power system following a generator tripping

The inertial response and the governor response come under the primary frequency control strategy. The primary frequency control action should respond to the fast frequency decline. The frequency nadir, i.e. the minimum frequency point, is mainly determined by the inertia. Inertia itself is determined by the rotating masses in the network. The governor action will stabilize the frequency but is unable to restore it without the support of the secondary control action, i.e. automatic generation control. Tertiary control will refill the reserves used for frequency restoration [6].

Conventional converter control strategies control the converter as a grid-connected current (or voltage) source. A typical converter controller arrangement, known as the decoupled controller, is shown in Figure 1.2.

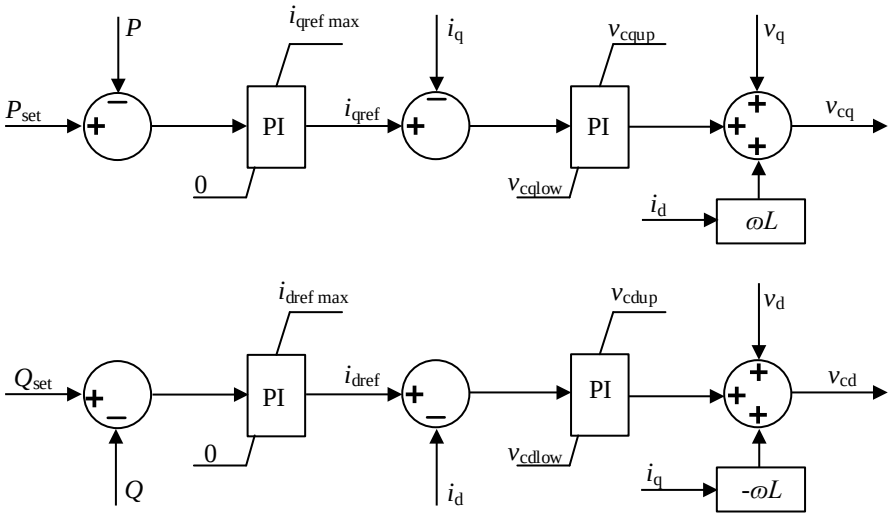

Figure 1.2 Vector control algorithm

The decoupled controller has an outer loop for power control and an inner loop for current control. The P_{set} and Q_{set} are the reference active power and reactive power values, respectively, which are compared with the measured active power (P) and reactive power (Q). Depending on the application, a converter terminal voltage controller may replace the reactive power controller and a dc voltage controller may be used instead of the active power controller. The external proportional-integral (PI) controllers output the converter current references in the dq0 domain. The ability to exert limits on the converter's current references is a major advantage of this method. The inner current controller together with limiters generates a signal to be used for converter's terminal reference voltages (v_{cd}, v_{cq}) generation. v_d and v_q are d and q components of the grid voltage, respectively. L is the line inductance between the converter terminal and the grid. The controller's close dependence on a phase-locked loop (PLL) is the main drawback of this scheme. Further, this control strategy provides power commands irrespective of the grid frequency and voltage. This inability to modulate the generated power is another concern with the conventional decoupled control strategy.

There are three main types of converter control strategies: (i) grid-forming converters are explicitly used in islanded mode to create and establish the grid voltage and frequency; (ii) grid-feeding converters cannot operate autonomously as they need a grid-former for synchronization (the decoupled-control strategy shown in Fig. 1.2 is a grid-feeding strategy); and (iii) grid-supporting converters, which have operability in both grid-connected and islanded modes [7].

There are numerous modern grid-frequency support platforms, which can be identified as either proven or emerging technologies. Synchronous condensers and modified wind-turbine controls are proven technologies. Synchronous condensers are synchronous motors without mechanical load whose generation or absorption of reactive power is controlled via their field excitation. Though a synchronous condenser is an established means of reactive power compensation, it provides added advantages over power-electronic based shunt compensators. Improvement of short circuit capacity, reduced sensitivity of the output reactive power to the grid voltage level variations, and the ability to exchange a small amount of kinetic energy with the system during power imbalances are among the notable advantages of synchronous condensers [8].

Wind is a leading RES. Frequency support by wind turbine has been mandated in many jurisdictions with sizeable wind generation such as in Quebec, Canada [9]. Doubly-fed induction generators (DFIGs) and permanent magnet SG (PMSG), which are commonly used wind turbine types, give frequency support via changing the injected power or the electromagnetic torque [10]. As the mechanism of power variation to grid-frequency variation is different from conventional SGs, the inertial response of wind turbines is different from that of SGs. There are active researches on supporting the gird frequency by wind turbines similar to a SG. The use of embedded energy storage systems (ESS) with wind turbine is one of them [10].

The emulation of inertial characteristics via an ESS is an emerging field of research. Capacitors, ultra-capacitors, batteries, and fuel cells are some of the possible ESS for frequency support. The dc link capacitor of converters support harmonic filtering, and can be used to control the dc link voltage or reactive power compensation [10]. The analogy between the stored mechanical (kinetic) energy in the rotating mass of a SM and the electrostatic energy in a capacitor is given below.

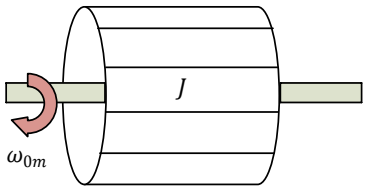

Figure 1.3 The rotor of a SM with a moment of inertia of J and nominal mechanical speed of ω_{0m}

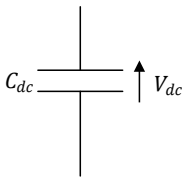

Figure 1.4 A capacitor with capacitance of C_{dc} and nominal voltage of V_{dc}

The inertia time-constant of the SM is given by (1.1):

$$H = \frac{W_{\mathrm{K}}}{S_{\mathrm{SM}}} = \frac{\frac{1}{2} J \omega_{0\mathrm{m}}^2}{S_{\mathrm{SM}}} \qquad (1.1)$$

where W_{K} is the rotor's kinetic energy at the rated speed (MW.s), J is the combined moment of inertia of the generator and turbine (kg.m^2), $\omega_{0\mathrm{m}}$ denotes the rated angular velocity in mechanical rad/s, and S_{SM} is the rated apparent power of the SM in MVA [8]. Similarly, the time-constant of the capacitor is given by (1.2):

$$\tau = \frac{W_{\mathrm{E}}}{S_{\mathrm{VSC}}} = \frac{\frac{1}{2} C_{\mathrm{dc}} V_{\mathrm{dc}}^2}{S_{\mathrm{VSC}}} \qquad (1.2)$$

where W_{E} and S_{VSC} give the electrostatic energy stored in the capacitor and the rated apparent power of the converter, respectively[5].

The capacitance C_{dc} and nominal voltage V_{dc} are analogous to the moment of inertia of the SM (J) and its nominal mechanical speed ($\omega_{0\mathrm{m}}$), respectively. Therefore, a particular inertia time-constant can be emulated by changing the dc voltage of the capacitor according to the grid frequency variation. The high-power density and the durability of ultra-capacitors make them ideal for cases where much larger inertial support is required than capacitors [10]. Fast charging and discharging capability makes battery energy storage systems (BESS) ideal to level the intermittent power output of RES [11]. The abundant energy generated by RES can be also used to generate hydrogen in electrolysers. In cases of power imbalances, hydrogen can be converted back to electricity using fuel cells in order to provide the needed frequency support [12].

Virtual synchronous machine (VSM) is an emerging concept in grid frequency support. VSM is a control strategy that modulates the output power of a grid-tied converter similar to a conventional SM. A mathematical model of the SM plays a central role in VSM algorithms. Therefore, from the grid's point of view the SM and VSM dynamics are similar [13]. Inertial and damping responses are two basic features that are emulated by most VSMs [14],[15]. The governor's response can be emulated via a frequency-droop based control loop. Therefore, emulated inertia and damping together with the droop action of the VSM can provide complete primary frequency control similar to a SM. To achieve these control objectives the converter must

be supported with a proper ESS in the dc side [16]. VSM has the potential for a number of applications. It provides a smooth transition between islanded and grid-connected modes in ac microgrid applications. Further, VSM-controlled HVDC systems can support weak ac systems interconnected to them. Bidirectional battery chargers can use VSM to facilitate vehicle to grid services [15].

1.2 Problem Definition

There are numerous types of VSM topologies suggested in literature. Some models have higher order representation of a SM while others are based on the classical model of a SM (swing equation-based second-order model). Additionally, VSM algorithms are different from one another based on the requirement of a PLL, controlling of the converter as a current source or a voltage source, field action emulation, over-current control ability, and many more ancillary services that can be provided. The control of a fast-acting power electronic converter as a slow acting electromechanical SM will risk some of the better performances that the converters have.

Most of the previous work in this area has been carried out in the grid connected mode, which may block the full observation of the unique features of the used VSM algorithm as the system voltage and frequency are set by the gird. Therefore, identification of the mostly required features for a VSM algorithm and possible extra features that can be added over the conventional SM dynamics is a much needed research focus. There is a lack of knowledge about the ways of manipulating the features of the VSM topology to obtain optimal dynamic responses. Therefore, this work is aimed to pave the way for applying appropriate VSM algorithms for the relevant application with a solid understanding of their comparative merits. The detailed switching model of VSM controlled converters allows to obtain the exact view of VSM operation.

1.3 Thesis Motivation

The VSM concept is still in its infancy. For proper application of these methods, potential users must have in-depth knowledge of these algorithms' true merits and shortcomings. This is the motivation to study the broad category of VSM algorithms using detailed comparative assessments. This analysis provides insight into the dynamic behaviour of the selected VSM algorithms.

1.4 Organization of the Thesis

The rest of the thesis is arranged as follows. Chapter 2 includes a thorough literature review on the existing VSM algorithms and explains the analogy between the conventional SM and VSM. Chapter 3 demonstrates the selected VSM algorithms. This includes the modifications that are included over the original algorithms. Detailed analysis of the large-signal stability characteristics is shown in Chapter 4, which also shows the test system developed in the PSCAD/EMTDC environment together with the obtained simulation results. Chapter 5 presents contributions, conclusions, and recommendations for future work.

Chapter 2 : VSM Topologies

2.1 Overview of VSM Topologies

The array of VSM algorithms consists of a number of controller arrangements. Though the initial efforts in VSM algorithm development focused on controller modifications, current focus is on the optimization of the appropriate control features. The available VSM algorithms have been broadly categorized and identified in several pieces of literature [13]-[15], [17]-[18]. The review of VSM algorithms in this chapter categorizes them into four basic groups depending on the mathematical model of the SM. These include (i) the droop-based model, (ii) swing equation based-model, (iii) full model, and (iv) simplified model. Figure 2.1 shows the arrangement of the converter connected system, which is referred in explaining those control topologies. v_o and i_o are respectively the measured voltage and current signals at the grid side. The active power and reactive power measured at this point is given by $P_{measured}$ and $Q_{measured}$, respectively. The current measurement at the converter terminal is given by i_{cv}. Z_g represents the impedance of the rest of the circuit connecting the inverter to the load.

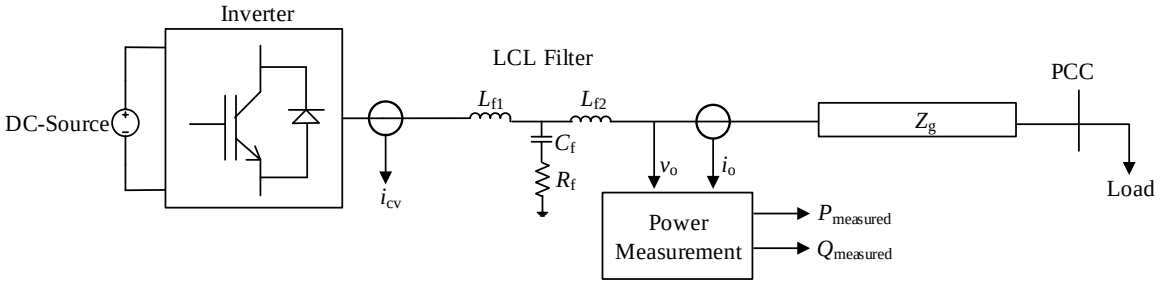

Figure 2.1 The arrangement of the considered system

2.1.1 Droop-based model

This type of controller algorithm does not explicitly mimic the mechanical or electrical dynamics of the SM. It is a commonly-used control architecture in micro-grid applications [19]. Under constant grid angular-frequency and active power reference, there is an equivalence between the swing equation and frequency droop control [19]. Power-frequency (*P*-*f*) droop and reactive power-voltage (*Q*-*v*) droop relationships are used to generate the phase angle and the magnitude of the reference voltage, respectively, for pulse-width modulation (PWM) switching actions of the converter that emulates the SM [20]. Figure 2.2 shows a schematic diagram of this

VSM controller. Cascaded internal voltage and current control loops, as shown in Figure 2.3, may also be added to ensure current and voltage regulation [7].

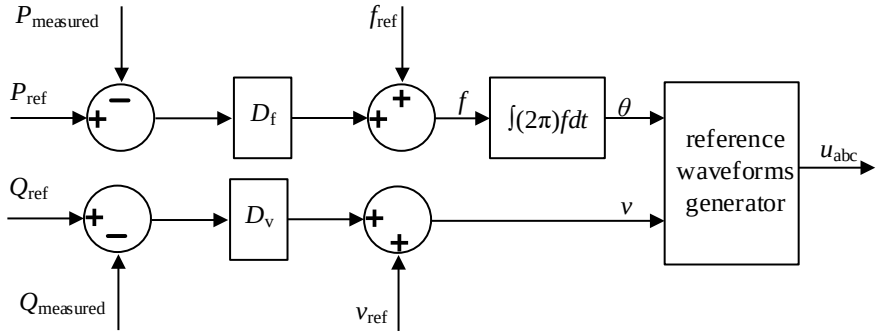

Figure 2.2 Droop-based controller without voltage and current controllers

In this scheme, the *P-f* loop generates the angular position of the reference signal (θ) by employing the target active power (P_{ref}), target angular frequency (f_{ref}), *f*-droop coefficient (D_f) and measured active power ($P_{measured}$). Similarly the *Q-v* loop uses the target reactive power (Q_{ref}), magnitude of target terminal voltage (v_{ref}), *v*-droop coefficient (D_v) and measured reactive power ($Q_{measured}$) to generate the magnitude of machine's terminal voltage (v). The controller arrangement without the internal voltage and current loops directly uses θ and v to generate the reference sinusoidal signals for PWM switching action.

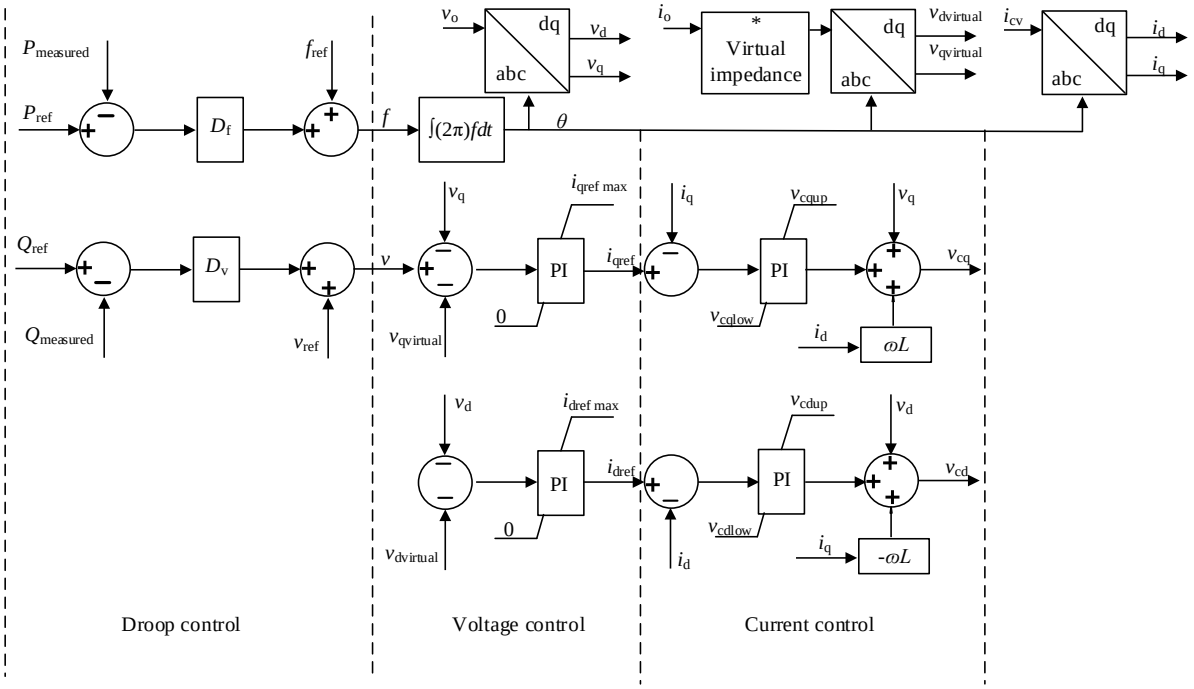

Figure 2.3 Droop based controller with voltage and current limiters

The cascaded controller structure uses the previously mentioned *P-f* and *Q-v* droop controllers to obtain the virtual angle (θ) and expected machine terminal voltage magnitude (v), respectively. θ will be used to obtain the relevant dq components of the voltages and currents. The expected machine terminal voltage (v), the dq components of the machine terminal voltage (v_d, v_q), and the voltage drop created artificially by the virtual impedance to obtain the converter current references in dq domain (i_{dref}, i_{qref}). To create a virtual voltage drop, a virtual impedance is multiplied by the grid current (i_o). The idea of using the virtual impedance is to create an inductance-dominant converter-grid connection, so that droop action works optimally [7]. The generated current references together with the dq components of the converter terminal current (i_d, i_q) will be utilized by the current controller to obtain the machine's terminal voltage signal in the dq domain (v_{cd}, v_{cq}). This is used for PWM switching action after converting to the abc domain.

2.1.2 Swing equation-based model

Compared with the droop-based controller, the swing equation-based controller has the conventional swing equation in the *P-f* control loop in order to obtain the angular position of a virtual rotor. This scheme allows to emulate the inertial and damping characteristics of a SM, which are important in shaping its transient response. The droop action can also be incorporated

into the model, allowing parallel operation of converters that are controlled using this scheme. Depending on how the magnitude of machine's electromotive force (emf) is obtained, variations of this scheme may be derived, namely the direct method, the cascaded method, and the use of swing equation to obtain power or current reference [18].

The direct method uses a separate reactive power or a voltage controller to obtain the emf amplitude [21]-[22]. Other than the active power, reactive power, frequency, and voltage controllers, some variants of the direct method have additional features over the conventional SM, taking advantage of power electronics. Low-voltage ride-through (LVRT) capability is one of these features that has been added on these VSM algorithms [22]. The phase angle and emf calculation paths of a direct VSM algorithm are given in Figure 2.4 and Figure 2.5.

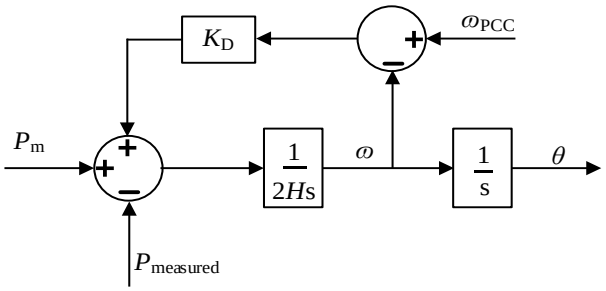

Figure 2.4 The phase angle calculation based on swing-equation

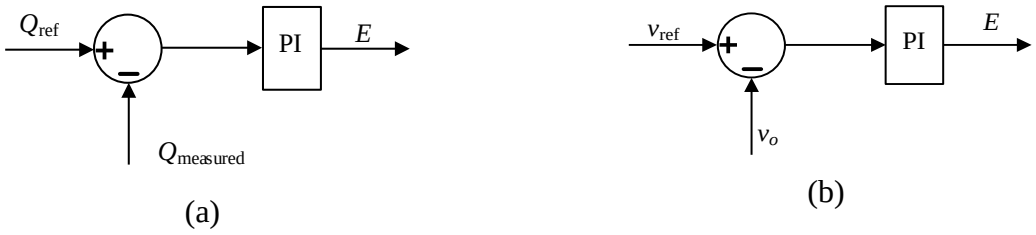

Figure 2.5 EMF magnitude calculation based on (a) *Q*-controller (b) *V*-Controller

P_m and $P_{measured}$ are the input active power (emulated mechanical power) and the measured active power, respectively. K_D and H are the damping co-efficient and inertia time-constant, respectively. The reactive power error signal, i.e., the difference between the reference reactive power (Q_{ref}) and measured reactive power ($Q_{measured}$) or the voltage error signal, i.e. the difference between the reference voltage (v_{ref}) and the measured voltage (v), can be used to generate the emf magnitude (E). PI controller can be used with the reference signal's magnitude generation, only

when single VSM is forming the grid. In parallel operation, P controller has to be used to avoid the hunting between the VSMs.

In order to allow more degrees of controllability, the cascaded structure has been introduced to the swing equation-based model as well. The external swing equation-based loop generates the virtual angular position, which is used to convert the voltage and current signals to the dq domain. The inner voltage controller generates the current references for the ensuing current controller, which in turn generates the machine's terminal voltage signal for PWM switching action [23]. Other than the inner voltage and current controllers, there are some VSM algorithms that use virtual impedance as well [16], [24]. The virtual impedance stage ensures an inductance-dominant converter interconnection. Figure 2.6 gives the latter converter topology [16].

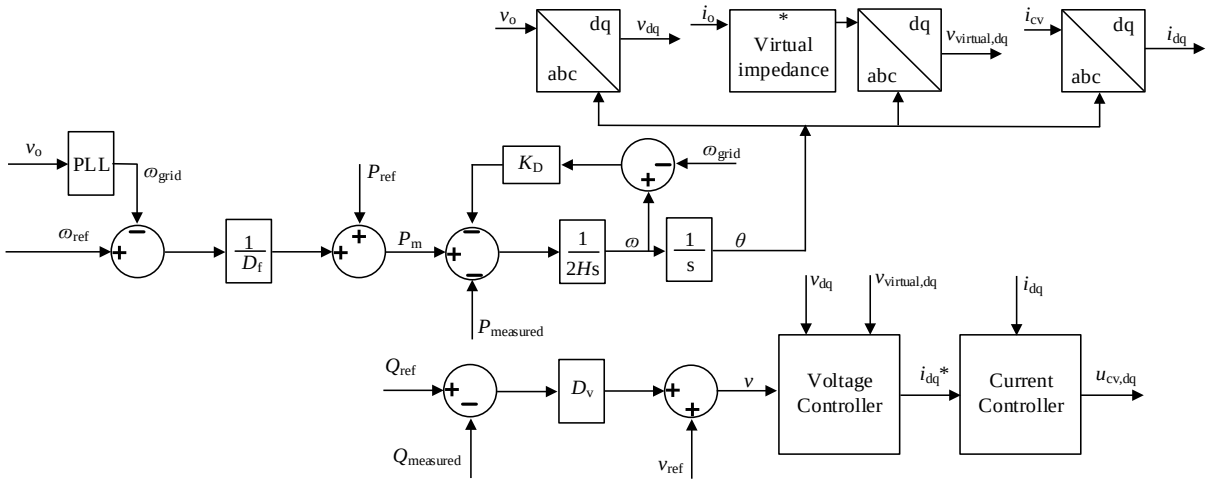

Figure 2.6 Swing equation based cascaded controller

The reference angular frequency (ω_{ref}), grid angular frequency measurement coming from the PLL (ω_{grid}), reference active power (P_{ref}), frequency droop co-efficient (D_f) have been used to generate the emulated mechanical power signal (P_m). Swing equation based inner controller uses the inertia time constant (H), damping co-efficient (K_D) along with the measured active power ($P_{measured}$) to generate a virtual angular position (θ). The Q-v droop block uses the virtual machine's terminal voltage reference (v_{ref}), reference reactive power (Q_{ref}), reactive power measurement ($Q_{measured}$), and the Q-v droop coefficient (D_v) to generate the expected magnitude of the machine terminal voltage (v). The virtual impedance block provides the same decoupling effect for P and Q controls, as mentioned before. This block generates the expected machine terminal voltage after

accounting for the voltage drop across the virtual impedance ($v_{virtual,dq}$). This signal together with the dq components of the gird side voltage (v_{dq}) will be processed by the voltage control block to generate the VSM's current references (i_{dq}^{*})The current controller utilizes this current signal with the dq components of the grid current (i_{dq}) to generate the machine's internal emf signal ($u_{cv,dq}$) for PWM switching action.

Some VSM algorithms explicitly use the swing equation to generate the power or current reference signals for converter controls [25]. The swing equation-based power controller is a part of the PLL used for grid-frequency measurement. This VSM algorithm has been modified for use with battery energy storage systems by adding the state of charge (SOC) as well [26].

2.1.3 Full model

The full model emulates not only the mechanical parts of a synchronous machine as in the above two controllers, but also the electrical parts thereof. The electrical model consists of flux linkages and includes the effect of damper windings. Though an exact SM is emulated, due to converter limitations this model is incapable of providing the same level of overcurrent protection as a conventional SM, unless the controller has a current control loop [15] as well. A VSM based upon the full model can be developed in either the abc [27]-[28] or dq domains [29]. The abc domain-based synchronverter model [27] controls the converter as a voltage source. The dq domain based Virtual Synchronous Machine Algorithm (VISMA) [29] controls the converter as a current source. The VISMA concept is illustrated in Figure 2.7

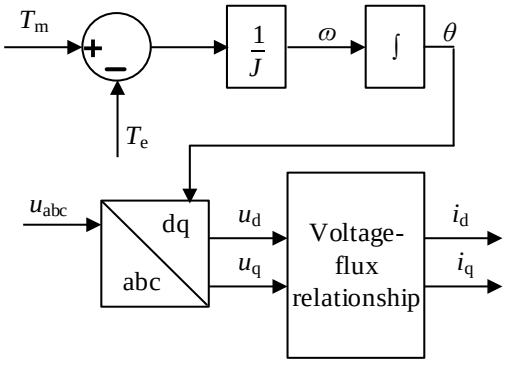

Figure 2.7 VISMA concept

The swing equation is used to obtain the phase angle (θ) for the park's transformation. The measured machine's terminal voltage together with the exciter voltage, self and mutual

inductances, and resistances of windings are used to generate the converter's current references. Hysteresis current control action is then used to control the converter.

2.1.4 Simplified model

In this model the rotor-stator electromagnetic coupling is neglected [18]. Virtual resistance and inductance are used to generate the machine's terminal voltage using the calculated emf [30].

2.2 A Comparison between a SM and a VSM

A VSM algorithm allows an intuitive operational analogy between a SM and a VSM-controlled power electronic converter. Different VSM algorithms provide different levels of information regarding the mechanical and electrical circuitry of a conventional SM. Assume a VSM algorithm with a swing equation-based direct PWM control. Figure 2.8 compares the grid-forming capability of a VSM controlled converter and a conventional SM.

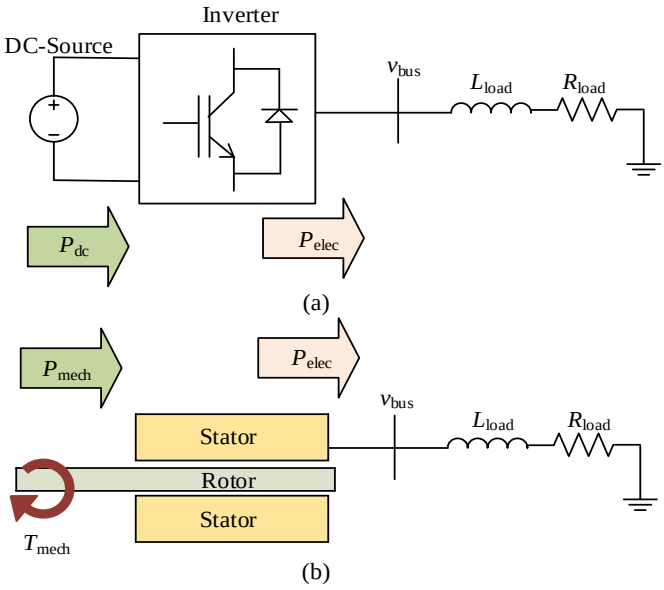

Figure 2.8 The comparison of grid forming capability of a (a) VSM, (b) SM

The VSM emulates similar characteristics to that of a SM, provided that the converter has a readily accessible dc system. This dc system can be a standalone ESS or a RES together with an ESS. The input mechanical power to a SM through its rotor is similar to the dc power input given to the converter. At steady state, the input mechanical power of a SM is equal to its output electrical power. Similarly, the input dc power of the converter will be equal to the electrical power output at steady state. A SM reaches a new steady state operating point by controlling its prime mover

settings according to the frequency droop settings, which in turn will control the mechanical power input to the SM. According to the virtual droop setting, the VSM will modulate its dc power by changing the duty ratios of power electronic switches. The response of a SM without the governor action is controlled by its inertia and damping values [8]. The transient response of a SM and VSM, which are based on the classical model of SM, are governed by the swing equation shown in (2.1).

$$\Delta P_{\mathrm{m}}-\Delta P_{\mathrm{e}}=2H\,\frac{\mathrm{d}(\Delta\omega_{\mathrm{r}})}{\mathrm{dt}}+K_{\mathrm{D}}(\Delta\omega_{\mathrm{r}}) \qquad (2.1)$$

where $\Delta\omega_{\mathrm{r}}$ gives the speed deviation of the rotor; ΔP_{m} is the change in the mechanical power input; ΔP_e is the non-frequency sensitive load change; K_{D} gives the load damping constant, which is typically between 1%-2%. This relates the change of the power of frequency-sensitive loads, such as motors, with the frequency deviation [8]. The inertia time-constant given by H is typically between 2-4 s for hydraulic units, while 2-ploe and 4-pole thermal units have inertia constants of 2.5-6 s and 4-10 s, respectively[8]. The large rotating mass of a SM's rotor takes care of the inertia value of the SM. For converters, an ESS with a sufficiently large power density and fast response time helps to emulate the inertial characteristics. Capacitors, super-capacitors, batteries, and flywheels are possible candidates for inertia emulation [31].

A synchronous generator (SG) faces three damping powers, namely field damping, induction damping, and load damping [32]. A typical rotor has two windings namely the field winding and amortisseur winding. Both of these windings will create electrical damping power following any disturbance according to Faraday's law. Load damping is created due to the frequency sensitivity of the connected loads. For example, under fault conditions, as the input mechanical power is greater than the output electrical power, the rotor will speed up. This component of power at slightly higher speed develops additional electrical power due to the characteristics of the connected system. This effect is reflected to the generator and produces damping in the generator. According to the classical model K_{D} is the load damping, which depends on the system of interest. In a VSM this is identified as a damping term, which may emulate either of the above three damping effects depending on the design of the controller. This is due to the fact that all the damping signals are proportional to the slip frequency. The required damping power for the VSM also needs to be supplied by some kind of energy source/sink used for inertia emulation.

In a SM the governor together with the turbine modulates the primary ESS to generate the required mechanical input power to meet the load-generation imbalance. Depending on the detail level of the governor-turbine's mathematical model, lead-lag compensator blocks can be added with relevant time-constants and gains. In particular, a slowly-responding hydraulic governor-turbine has negligible significance in transient stability analysis, unless in the study of a small isolated system [8]. In order to ensure proper sharing of power between parallel-connected units, the droop or speed regulation is provided with the governor. The *P-f* droop relationship is given by (2.2).

$$f = f_{\text{set}} + D_{\text{f}}(P_{\text{set}} - P) \tag{2.2}$$

where f_{set} and P_{set} are target system frequency and active power values, respectively. The actual active power (P) and frequency (f) are controlled by the linear *P-f* droop gain (D_{f}). A typical value for the *P-f* droop is 5% [8]. The VSM algorithm can emulate governor-turbine action with a virtual droop value and relevant lead-lag compensator blocks, whose gains and time-constants can be arbitrarily selected. The converter should be accompanied with a slow acting, energy dense ESS in order to emulate governor-turbine characteristics.

The primary intention of the exciter of a SM is to maintain the machine's terminal voltage and reactive power loading. Some auxiliary service providers such as power system stabilizers, load compensators, limiters, and protective circuits have also been incorporated with the exciter [8]. A VSM can emulate the exciter action with appropriate lead-lag compensators and a voltage controller without constraint exerted by the physical limitations of a SM. The load compensator of a SM's exciter uses an adjustable resistance and an inductance to emulate the impedance between the machine's terminal and the rest of the system. This acts as a reactive voltage-current (v- i) compensator to ensure parallel reactive load sharing [8]. The SMs can operate in parallel even without this load compensator action as the reactive power sharing is controlled by the reactance of transformer and transmission line connecting to the rest of the system. VSM algorithms that use virtual impedance use this *v-i* regulation [16], [22]. There are VSM algorithms built upon reactive power-voltage (Q-v) regulation given in (2.3) [20].

$$v = v_{\text{set}} + D_{\text{v}}\left(Q_{\text{set}} - Q\right) \tag{2.3}$$

where v_{set} and Q_{set} give the target voltage and reactive power values, respectively. The voltage droop coefficient (D_v) controls the reactive power (Q) and voltage (v) to achieve the desired parallel operation. This Q-v droop can also be used to modulate the reference voltage signal to the exciter of SM, so that the machine's terminal voltage is maintained at the required value while supplying the proper reactive power portion. While a specific circuit controls the dc current flowing to the field of a SM [8], a VSM changes the modulation index of the reference signal so as to control the switching pattern to supply the required reactive power.

Chapter 3 : Major VSM Algorithms

In this chapter a detailed description is given for the selected four VSM algorithms, namely, virtual synchronous machine zero inertia (VSM0H) model, voltage controlled-VSC (VC-VSC) model, modified-VSM0H model, and synchronverter model. In the studies in this chapter, the controllers are tested for grid-forming capability, while assuming a readily accessible dc-side source/sink for the converters. Additionally, all the controllers are developed in the per-unit basis.

3.1 VSM0H Model

VSM0H model comes under the droop-based VSM algorithm category. This model uses conventional *P-f* and *Q-v* droop control loops to obtain the target frequency and voltage of the machine terminal voltage, respectively [20]. VSM0H model controls the converter as a voltage source. The controller transfer function is first order and, therefore, introduces a purely damped response compared with the conventional second-order damped oscillations given by a physical SM [33]. A key feature of the VSM0H is the absence of a PLL. Though the original work has another filter for damping the calculated power signal, this thesis ignores it on the basis of insignificant added advantage. A boxcar filter (moving average filter) has been used in the previous work to filter out the instantaneous power values. The boxcar filter acts as a low-pass filter with zeros at every integer multiple of $1/T$, where T is the window size [34]. These filter zeros can be easily adjusted by changing the window size. For example, $T = 1/60$ s means zeros appears at every multiple of 60 Hz, and the filter is properly tuned to measure signals with the fundamental frequency of 60 Hz. This thesis uses a low-pass filter with a bandwidth of 60 Hz, which removes the higher order harmonics and results in a much simpler controller topology. VSM0H acts as an "infinite-inertia" system for harmonics and unbalances, which helps to maintain the point of common coupling (PCC) voltage and power quality. The controller composition is given in Figure 3.1.

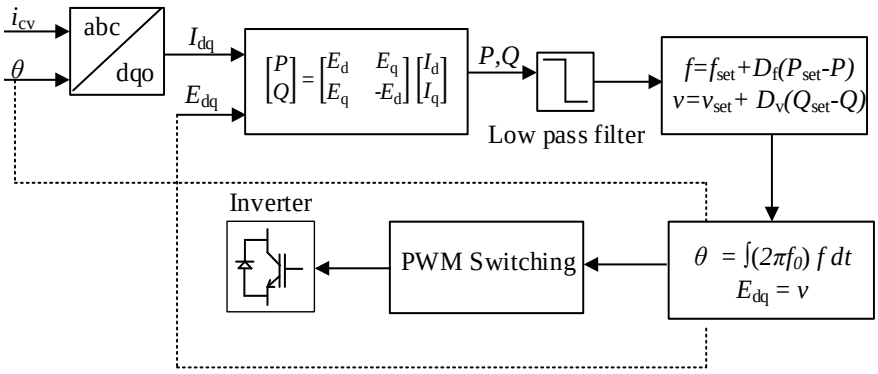

Figure 3.1 VSM0H model

The only required measurement is the current flowing through the converter (i_{cv}). The target frequency (f_{set}), the target voltage (v_{set}), the set active power command (P_{set}), the set reactive power command (Q_{set}), frequency droop coefficient (D_f) and voltage droop coefficient (D_v) should be supplied externally. Inbuilt droop action facilitates parallel operation of VSM0H controlled converters.

Though VSM0H model avoids explicit emulation of inertia, the *f*-droop coefficient, together with the time constant of the first-order low-pass filter, emulates equivalent inertial and damping effects. The low-pass filter creates a delay in the power signals, which is mathematically equivalent to inertial effects [17], [13]. The proof given in [13] is repeated here for convenience. Figure 3.2 shows the frequency droop control block.

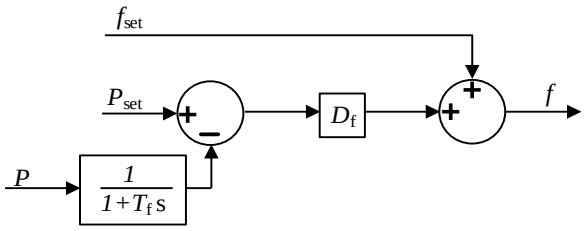

Figure 3.2 Frequency droop control block

T_f is the time constant of the low-pass filter. The other parameters have the same interpretation as above. The relationship of Figure 3.2 can be given as below.

$$f = f_{set} + D_f\left(P_{set} - \frac{P}{(1+T_f s)}\right) \tag{3.1}$$

Assuming a constant P_{set},

$$P_{\text{set}}\text{-}P = \frac{T_{\text{f}}}{D_{\text{f}}}\text{s}.(f\text{-}f_{\text{set}}) + \frac{1}{D_{\text{f}}}(f\text{-}f_{\text{set}}) \tag{3.2}$$

The rearranged *f*-droop given in (3.2) is comparable with the swing equation given in (2.1). Therefore, the inertia time constant is proportional to $T_{\text{f}}/D_{\text{f}}$ and damping co-efficient is proportional to $1/D_{\text{f}}$. However, the lag time of the conventional droop control is smaller (around several milliseconds) which compares to the lag time required to emulate inertial and damping effects (around several hundred milliseconds) to impact electro-mechanical oscillations [23]. Therefore, care should be exercised in selection of the filter's time constant.

Due to the absence of any control action to restore the VSM's terminal voltage, this controller does not emulate the exciter action of a SM. The dynamic responses of the controller for large signal disturbances will be discussed in the next chapter.

3.2 VC-VSC Model

VC-VSC is a swing equation-based direct-type VSM algorithm (Figure 3.3). Other than the *f*-droop, the VC-VSC has the swing equation-based control loop in its *P*-*f* controller [35]. Therefore, VC-VSC model can emulate both the artificial inertial and damping effects. The reference frequency (f_{set}) and grid frequency (f_{pcc}) are linked with the *f* -droop co-efficient (D_{f}) to modulate the virtual active power reference signal (P_{set}). The output signal of this stage is the emulated mechanical input power of the VSM (P_{m}). The inner controller modifies this input power signal and the measured active power signal (P_{measured}) according to the swing equation to generate the angular position of the reference signal (θ). The nominal frequency, f_0, is used to obtain the rotational angular speed from the per-unitized frequency. The inertia time constant (H) and damping co-efficient (K_{D}) can be selected arbitrarily. The damping path does not contribute to the grid-forming mode, as the angular frequency at PCC is the same as the virtual machine speed, *f*. Therefore, instead of the external frequency measurement the VSM speed can be used. The *Q*-*v* controller uses the reference reactive power (Q_{set}), measured reactive power (Q_{measured}), reference voltage (v_{set}), and *v*- droop co-efficient (D_{v}) to obtain the expected magnitude of the terminal voltage (v) according the *v*-droop relation. The generated voltage is used to find out the modulation

index. Then the modulation index, together with the virtual phase angle generated from the *P-f* controller, is used to generate the reference waveforms for the PWM switching action.

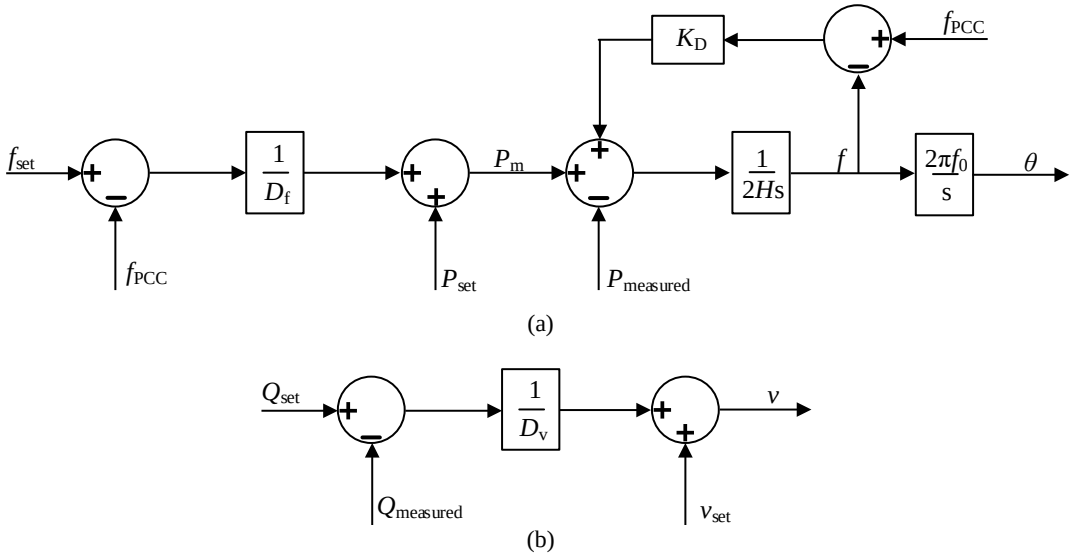

Figure 3.3 VC-VSC model (a) *P-f* controller, (b) *Q-v* controller.

Previous work on this concept has neglected the Q_{set} in the voltage droop block. This has been added in this work. The original work has a separate path to control the reactive power in the grid-connected mode. The objective of voltage control depends on the mode of operation, i.e., the grid determines the voltage in the grid-connected mode and only the set reactive power needs to be met. In the isolated mode, the voltage must be formed and maintained by the controller and cannot be used to regulate the reactive power. In transition from grid-connected to islanded, the path used to control reactive power is removed by setting the gain of the control loop to zero. Therefore, this controller requires a modification at every instant of mode shift between grid-connected and islanded modes. Since this study focuses on grid-forming capability, the reactive power controlling loop is removed from the *Q-v* controller. The developed islanding detection and over-current limiting actions in the original work are also excluded to create a fair comparison between other tested VSM algorithms. The absence of the emulated field action avoids the restoration of the terminal voltage. This avoids the emulation of SM dynamics optimally in this model as well. Only the transient responses of active power and system frequency will be changed from the VSM0H model, due to the inner controller part based on the swing equation of the *P-f* controller. The steady state response, which will depend on the droop action, will be same for VSM0H and VC-VSC models. One way of taking measurement is via a PLL.

3.3 Modified-VSM0H Model

The authors of the VSM0H model, which depends only on the droop control action, improved its mathematical model and introduced the modified-VSM0H model [33]. The modified VSM0H model also comes under the swing equation-based VSM category. The *P-f* control loop consists of the *f*-droop with a PI controller, which generates the emulated governor signal for the swing equation-based inner control path to generate the angular position of the reference signal. The original work uses a first-order low-pass filter with a gain and time constant to mimic the gain and time delay of the mechanical governor system, respectively. This has been ignored in this study as this further slows down the converter's response and jeopardizes the inherent fast acting capability of the converters. Though the previous work has introduced several damping signals for the swing equation-based control path, this work has used only a single damping signal with a damping co-efficient that is comparable with other controllers tested in this work.

The *Q-v* controller has rearranged the *v*-droop with a PI controller to generate the modulation index of the reference voltage signal. In the original work, the PI controller output has been passed through a first-order low-pass filter, which emulates the gain and time constant of the field of the SG. This low-pass filter has been ignored to ensure a faster controller performance. The dynamic braking and over-current control, which were in the original work, have been ignored in this analysis in order to facilitate a fair comparison. The original work has expanded the EMT model to an RMS model. This work will only focus on the EMT model as the interest is on the detailed transient and steady state responses than system level studies. The controller topology used in the analysis is given in Figure 3.4.

The PI controller of the *P-f* controller uses the active power command (P_{set}), system frequency command (f_{set}), active power measurement ($P_{measured}$), system frequency (f_{PCC}), which is similar to the angular frequency in pu, together with the slope of the *f*-droop characteristic (D_f) to emulate the mechanical power signal (P_m). The swing equation-based control section requires inertia time constant (H) and damping co-efficient (K_D) to generate the virtual rotor's speed (f) and the phase angle (θ). f_0 is the nominal frequency. One key observation that can be made regarding the controller topology is the use of active power measurement in both the external and internal controllers of the *P-f* loop. The PI controller of the *Q-v* control loop uses the reactive power command (Q_{set}), voltage command (v_{set}), measured voltage (v_o), measured reactive power

($Q_{measured}$) and the *v*-droop co-efficient (D_v) to generate the modulation index of the reference signal (*MI*).

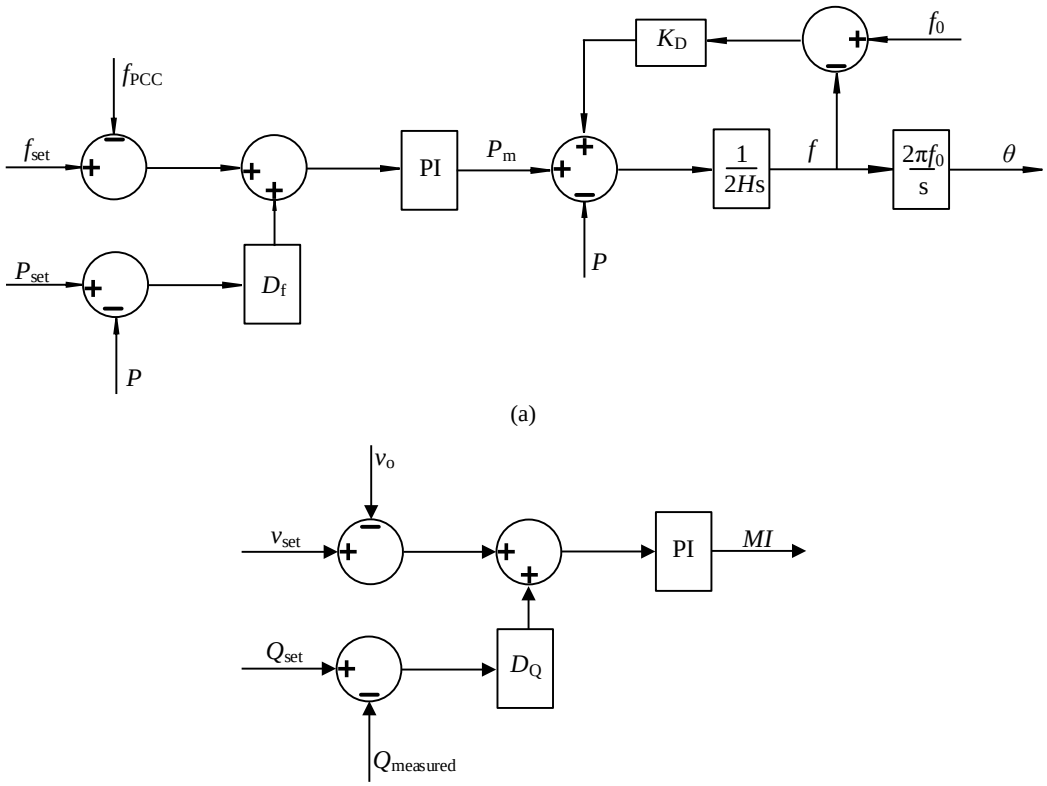

Figure 3.4 The modified VSM0H model (a) *P-f* controller, (b) *Q-v* controller.

For a stable controller operation, the *Q-v* controller's integral time-constant should lie above the integral time-constant of the *P-f* controller. To avoid interactions between the inner and outer control loops the PI controller's time-constant in the *P-f* controller should stay above the time constant of the swing equation-based internal controller. The swing equation-based loop can be easily scaled down to a first-order low-pass filter with the gain of $1/K_D$ and time constant of $2H/K_D$. Therefore, PI controller time constants have to be changed with the arbitrary selection of *H* and K_D.

3.4 Synchronverter Model

This VSM algorithm falls under the full-order model category, which emulates both the mechanical and the electrical models of SM. Although the SG model is well known, a brief explanation is given for the consistency and also for the convenience of the reader [27].

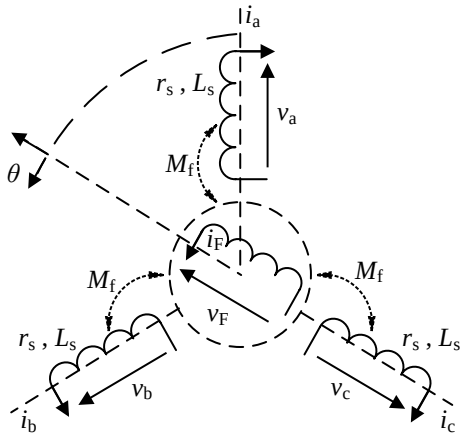

Figure 3.5 An idealized two-pole, round rotor SG representation.

As shown in Figure 3.5, the considered SG is a two-pole, round rotor machine without damper windings, saturation phenomena, eddy current effects, and magnetic coupling between stator windings. The mechanical speed of the rotor is equal to its electrical speed of it. With the stator phase currents as $\mathbf{i}=[i_a,i_b,i_c]^T$, self inductance of each stator coil (L_s), winding resistance of each coil (r_s), the machine terminal voltages $\mathbf{v}=[v_a,v_b,v_c]^T$ can be found out by Faraday's law.

$$\mathbf{v} = -r_s\mathbf{i} - \frac{d\phi}{dt} \tag{3.3}$$

The stator flux linkages $\phi=[\phi_a, \phi_b, \phi_c]^T$ can be obtained by 3.4.

$$\phi = L_s\mathbf{i} + M_f i_f \widetilde{\cos\theta} \tag{3.4}$$

where θ is the rotor angle, M_f is the maximum mutual inductance between a stator winding and the field winding, i_f is the field current, and $\widetilde{\cos\theta}=[\cos(\theta), \cos(\theta - 2\pi/3), \cos(\theta + 2\pi/3)]^T$. With constant i_f and using (3.3) and (3.4), the machine's terminal voltage, v, and internal emf ($\mathbf{e}=[e_a,e_b,e_c]^T$) can be obtained as below.

$$\mathbf{v}=-r_s\mathbf{i}-L_s\frac{d\mathbf{i}}{dt}+\mathbf{e} \tag{3.5}$$

$$\mathbf{e}=M_f i_f \dot{\theta}\widetilde{\sin\theta} \tag{3.6}$$

The PWM switching action uses e as its reference signal to control the converter as a voltage source. The rotor angle is obtained via the swing equation. For that, the required equivalent electrical torque signal is obtained after considering the energy stored in the magnetic field (3.7).

$$T_e=M_f i_f\left(i_a\sin(\theta)+i_b\sin(\theta-{}^{2\pi}/_{3})+i_c\sin(\theta+{}^{2\pi}/_{3})\right) \tag{3.7}$$

$M_f i_f$ is obtained via a Q-v controller. The generated reactive power is given by 3.8.

$$Q=-\dot{\theta}M_f i_f\left(i_a\cos(\theta)+i_b\cos(\theta-{}^{2\pi}/_{3})+i_c\cos(\theta+{}^{2\pi}/_{3})\right) \tag{3.8}$$

For clarity, the controller block diagram is given in Figure 3.6. The calculation block uses the measured converter output current (i_{cv}), the phase angle (θ) generated by the P-f controller and the Q-v controller generated $M_f i_f$. As explained in section 3.1, the damping path can be explicitly used to emulate the droop action, given a constant active power reference. Therefore, the synchronverter uses the damping path to emulate the f-droop action using per unitized nominal angular frequency ($\overline{\omega_n}$), VSM angular frequency (ω), and the f-droop co-efficient (D_f). Active power reference (P_{set}), per unitized nominal angular frequency ($\overline{\omega_n}$) are used to mimic the mechanical torque (T_m); ω_n is the actual nominal angular frequency.

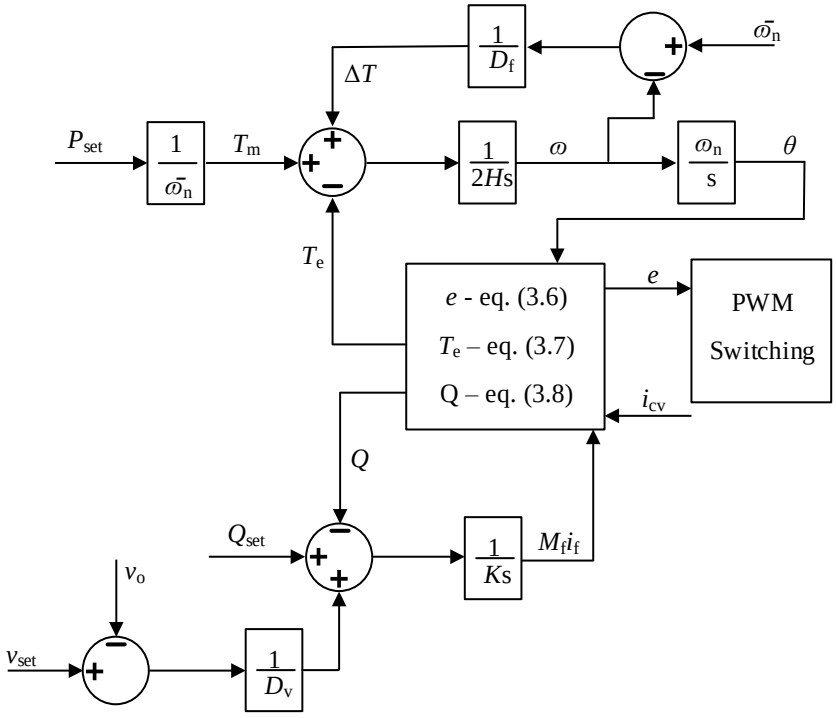

Figure 3.6 The synchronverter model

T_m signal is used with the calculated electrical torque signal (T_e) and the torque difference created due to the droop action (ΔT) to obtain θ using an arbitrary inertia time constant (H). The Q-v controller uses the measured terminal voltage (v_o), calculated reactive power (Q), target voltage (v_{set}), target reactive power (Q_{set}), and the v-droop coefficient (D_v) to obtain the $M_f i_f$ signal through an integrator with a time constant of K. For a stable controller operation, the Q-v controller's time constant, KD_v/ω, should be larger than the P-f controller's time constant of $2HD_f$.

The synchronverter is improved by integrating the synchronization function to the controller itself and removing the need for a PLL [28]. As a PLL is a non-linear slow-acting external control loop, the removal of PLL improves the controller performances in terms of accuracy and efficiency. Though the self-synchronizing synchronverter cannot be used for grid-forming scenario, as it requires an external grid to synchronize with, this has been summarized here for the completeness. Figure 3.7 gives the controller block diagram of the self-synchronizing synchronverter.

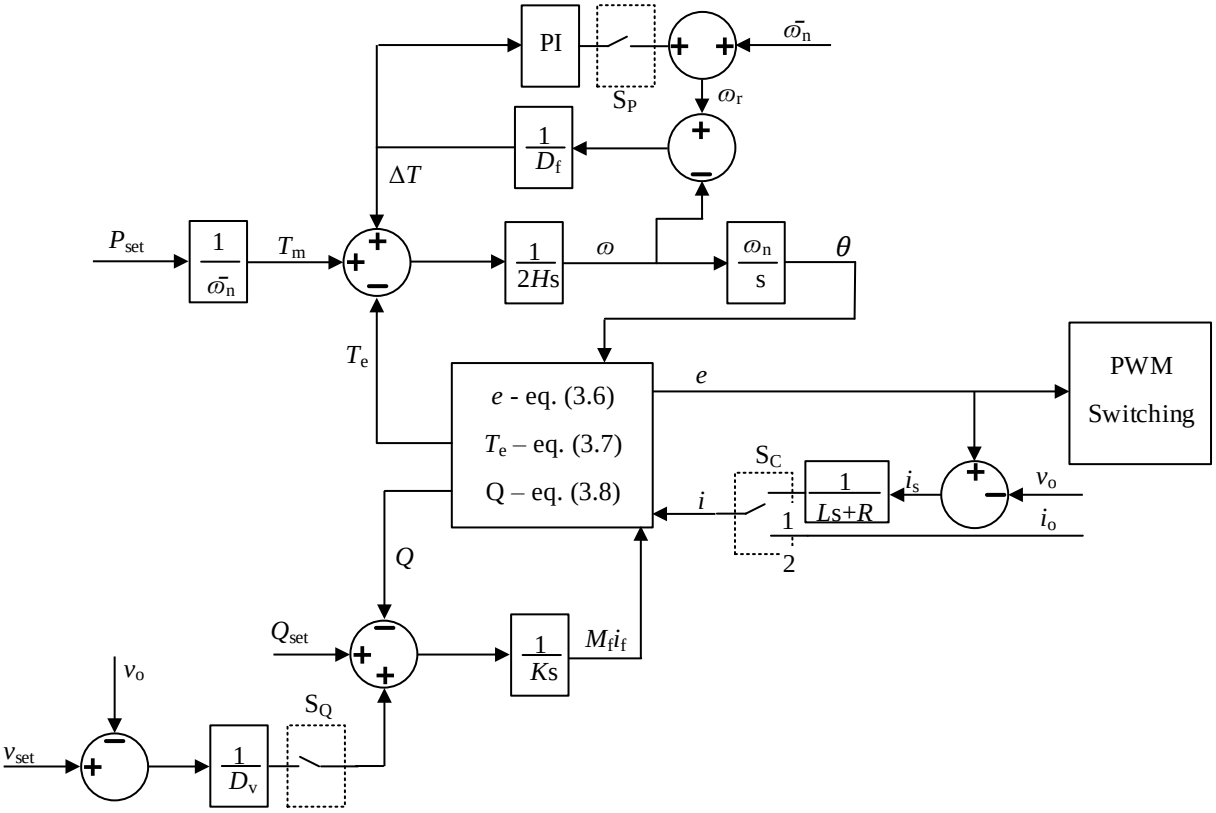

Figure 3.7 Self-synchronizing synchronverter

There are only three modifications compared to the original synchronverter model. Namely, the virtual current feed part, which comprises of the low-pass filter and the S_c switch, the PI controller path with the S_p switch, and the S_Q switch in the *Q*-*v* control loop. While a detailed explanation is given in [28], this will restate the roles of the newly added features. The series connected virtual inductance (L) and virtual resistance (R) generate a virtual current (i_s) flowing between the VSM terminal and the PCC. The point at which i_s=0, makes the instantaneous machine terminal voltage (e) and the instantaneous PCC voltage (v_o) the same. At this point synchronverter is ready for grid integration and S_c should be at position 1 with S_P-on, S_Q-off, P_{set}=0 and Q_{set}=0. After grid connection the S_P and S_Q switch positions will create four unique operation modes.

Chapter 4 : Detailed Assessment

The aforementioned four VSM algorithms have been tested in PSCAD/EMTDC. System modeling and simulation results are presented in the following sections.

4.1 Study System

As given in Figure 4.1, the study system consists of a detailed switching model of a two-level VSC connected to a load via an LCL filter, a step-up transformer, a short transmission line of 10 km length. The parameters of the test system and the short transmission line are given in Table 4.1 and Table 4.2, respectively. Constant P loads and constant L loads are used in the test system. A nominal frequency (f_0) of 60 Hz is used throughout the simulations.

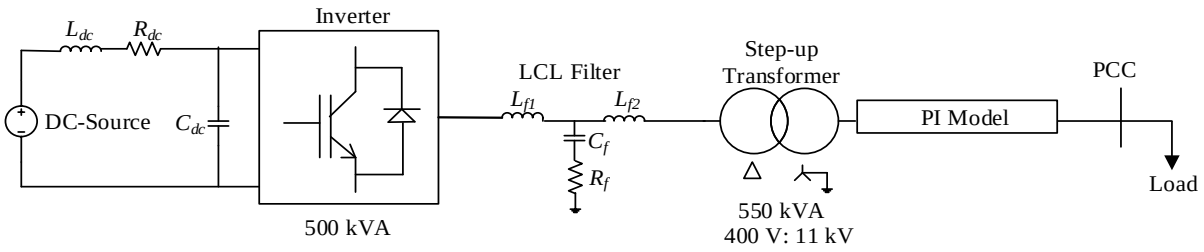

Figure 4.1 Single-line diagram of the study system

Table 4.1 Parameters of the study system

Parameter	Value	Parameter	Value
dc voltage	4 kV	L_{f1}	150 µH
R_{dc}	0.0006 Ω	L_{f2}	5 µH
L_{dc}	0.1 H	C_f	828.93 µF
C_{dc}	312.5 µF	R_f	0.08 Ω
converter rating	500 kVA	transformer leakage reactance	0.1 pu
fixed-P component of load	0.6 pu	fixed-Q component of load	0.6 pu

Table 4.2 Parameters of the short transmission line

Parameter	R_1 (Ω/km)	X_1 (Ω/km)	Y_1 (µS/km)	R_0 (Ω/km)	X_0 (Ω/km)	Y_0 (µS/km)
Value	0.103	0.405	4.117	0.279	1.902	0

The detailed switching model of the converter is used to observe the impact of high frequency switching phenomena. The LCL filter is used to reduce the current harmonics below the standard value of 5% (according to IEEE 1547 standard). The selected 4 kV is overrated, which can be reduced to a value that allows the converter to generate the required ac output voltage. This will realise a more practical test system.

4.1.1 Inverter

A two-level VSC with six pairs of anti-parallel IGBTs and diodes is used to model the inverter as given in Figure 4.2(b). Sinusoidal PWM (SPWM), which is used to generate the switching signals (S_1, S_2, …S_6), compares the reference waveform generated by the VSM algorithm with a high frequency saw-tooth carrier signal of 2 kHz (Figure 4.2(a)). The converter's dc side is modeled using an ideal dc voltage source connected in series with an inductor and a resistor together with a shunt dc link capacitor. The dc link capacitor is sized using the general heuristic rule of 5 kJ/MVA. The line inductance and resistance are set in order for the dc current ripple to be less than 4% and to adhere to typical line parameters [36], respectively. The converter terminal output phase voltages (v_a, v_b,v_c) consist of fundamental components plus higher order harmonics. The fundamental output phase voltages are given by (4.1) – (4.3). The modulation index (m) and the phase angle (ωt) are given by the VSM algorithm.

$$v_{a,f} = m\frac{V_{dc}}{2}\sin(\omega t) \tag{4.1}$$

$$v_{b,f} = m\frac{V_{dc}}{2}\sin\left(\omega t - \frac{2\pi}{3}\right) \tag{4.2}$$

$$v_{c,f} = m\frac{V_{dc}}{2}\sin\left(\omega t + \frac{2\pi}{3}\right) \tag{4.3}$$

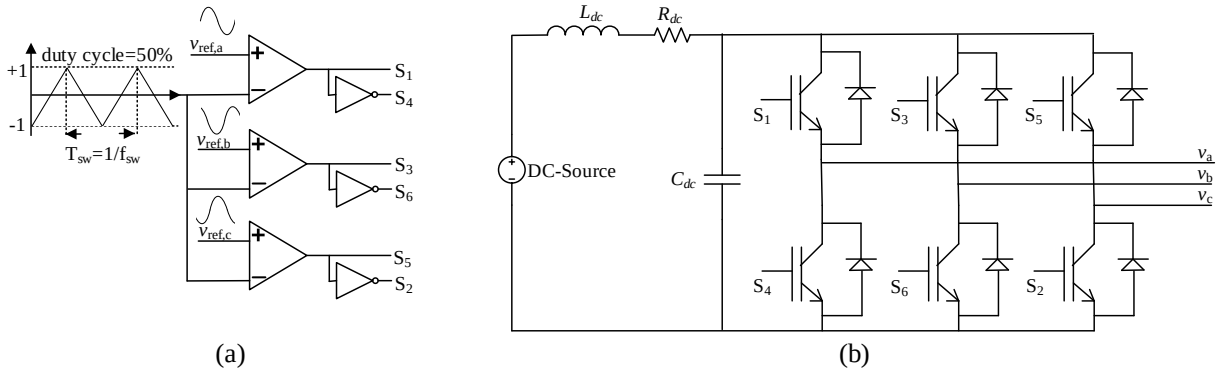

Figure 4.2 (a) The SPWM generator (b) Two-level VSC arrangement

One advantage of the SPWM is that its harmonic content, which depends on the carrier ratio (the frequency ratio between the switching signal and the reference signal) is pre-known. The LCL filter design procedure is explained in the next section.

4.1.2 LCL filter

L-filter, LC-filter and LCL-filter are three popular passive filter configurations employed in three-phase inverters. The L-filter is a first-order filter that uses a single inductor in series with each converter terminal. For proper harmonic elimination, it will require a higher order switching frequency, which is normally above 20 kHz [37]. The second-order LC-filter uses a shunt capacitor with the series connected inductor to ensure further attenuation of the higher order harmonics. With stiff grids, the shunt branch becomes ineffective and the output current ripple will be same as the inductor current ripple. In most application there exists a transformer with a leakage inductance. This inductance together with the LC filter results in an LCL filter. However, the effective grid impedance is a variable, which will cause unforeseen variations in the filter performance. Therefore, in LCL-filter design procedure, an additional inductor is normally added in the grid side to reduce this dependency.

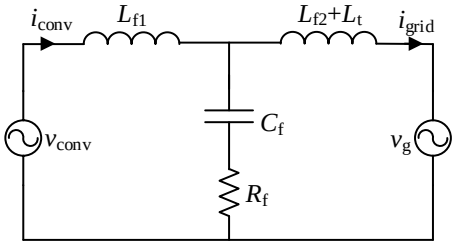

Figure 4.3 The single-line diagram of the LCL filter connecting VSC and the grid.

The LCL filter consists of converter side inductance (L_{f1}), gird side inductance (L_{f2}), transformer leakage reactance (L_t), filter capacitor (C_f), and damping resister (R_f). Among damping circuits, the series connection of a resistor with the shunt capacitor is a simple method [37]. As the converter generates higher order harmonics and the LCL filter suppresses them, at higher order harmonics the converter can be identified as a harmonic generator and the grid as a short circuit [38]. Therefore, the filter transfer function between the output current and the input voltage is as in (4.4).

$$\frac{i_{grid}}{v_{conv}} = \frac{1+C_f R_f s}{L_{f1}(L_{f2}+L_t)C_f s^3+(L_{f1}+L_{f2}+L_t)C_f R_f s^2+(L_{f1}+L_{f2}+L_t)s} \tag{4.4}$$

It can be shown that the resonance frequency is equal to $\frac{1}{2\pi}\sqrt{\frac{L_{f1}+L_{f2}+L_t}{L_{f1}(L_{f2}+L_t)C_f}}$. There are a number of LCL filter design approaches, which commonly use constraints such as the THD value of the grid current, reactive power consumption, allowable current ripple, and resonance frequency [39]. After considering the reactive power ceiling value for the capacitor as 10% of the converter rating, the capacitor value is obtained as 828.90 μF. To limit the voltage drop during the normal operation the total inductance is retarded [38]. The resonance frequency is designed to lie between ten times the line frequency and the half of the switching frequency; therefore, it properly attenuates the harmonics of the order of switching frequency. As L_t=77 μH, the remaining inductors are set as L_{f1}=150 μH, L_{f2}=5 μH. Then, the resonance frequency will be 760 Hz, which is in the required range. The damping resistance value is normally selected as one third of the filter capacitive impedance at the resonant frequency [38]. Therefore, R_f is set to be at 0.08 Ω. With the set inductor/capacitor values, the converter maintains the THD of the grid current well below the required 5% with insignificant voltage drop across it. Figure 4.4 shows the current flowing through the filter capacitor following a three-phase to ground solid fault at PCC with VSM0H in service. This shows how the presence of the damping resistor has damped out the higher order frequencies which are flowing through the shunt branch.

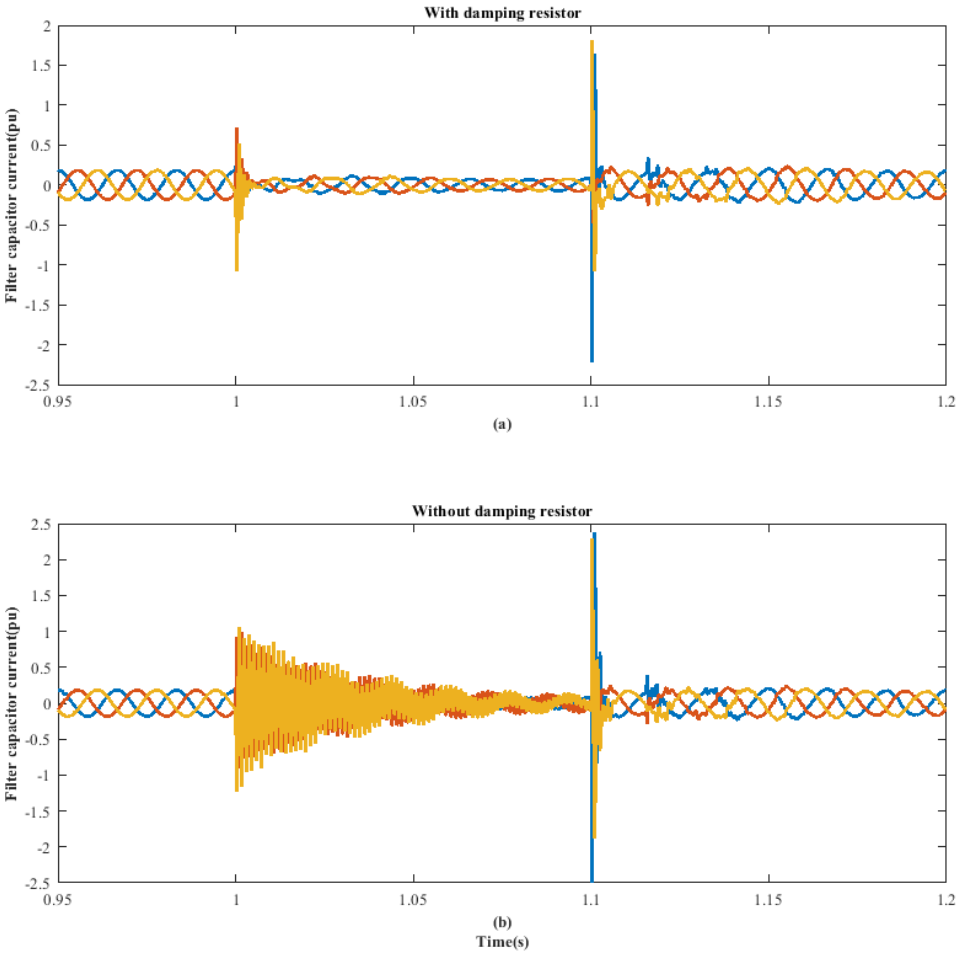

Figure 4.4 The effect of damping resistor on the LCL filter performance

Four types of tests, namely a step change in constant P load, a step change in constant L load, solid three-phase-to-ground fault at the PCC, and a high impedance three-phase-to-ground fault that will drop the PCC voltage to 50% are carried out to observe the SM and VSM dynamic responses for large-signal disturbances.

4.2 SM Time-Domain Simulation Results

To compare the performance of VSM algorithms against the conventional SM, a 500 kVA SM is connected instead of the VSM to the test system given in Figure 4.1. The parameters used for the SM model are given in Table 4.3. The ACIA exciter parameters are given in Table 4.4. A turbine of non-elastic water column without surge tank type is used and its parameters are given in Table 4.5. The hydro governor parameters are given in Table 4.6

Table 4.3 The SM parameters

Parameter	Value	Parameter	Value
Rated RSM line-to-neutral voltage	0.23094 kV	Base angular frequency	376.992 rad/s
Rated RMS line current	0.722 kVA	Inertia constant	3 s
Terminal voltage magnitude	1.075 pu	Mechanical friction and windage	0.05 pu
Armature resistance (R_a)	0.0051716 pu	Potier reactance (X_p)	0.163 pu
Unsaturated reactance (X_d)	1.014 pu	Unsaturated transient reactance (X_d')	0.314 pu
Unsaturated transient time (open) (T_{do}')	6.55 s	Unsaturated sub-transient reactance (X_d'')	0.28 pu
Unsaturated sub-transient time (open) (T_{do}'')	0.039 s	Unsaturated reactance (X_q)	0.77 pu
Unsaturated sub-transient reactance (X_q'')	0.375 pu	Unsaturated sub-transient time (open) (T_{qo}')	0.071 s

Table 4.4 AC1A Exciter parameters

Parameter	Value	Parameter	Value
Lead time constant (T_C)	0.0 s	Rate feedback gain (K_F)	0.03 pu
Lag time constant (T_B)	0.0 s	Rate feedback time constant (T_F)	1.0 s
Regulator gain (K_A)	400.0 pu	Exciter time constant (T_E)	0.8 s
Regulator time constant (T_A)	0.02 s	Exciter time constant related to field (K_E)	1.0 pu
Field circuit commutating reactance (K_C)	0.2 pu	Demagnetizing factor (K_D)	0.38 pu
Saturation at VE1 (SE (VE1))	0.10 pu	Exciter voltage SE1(VE1)	4.18 pu
Saturation at VE2 (SE (VE2))	0.03 pu	Exciter voltage SE2(VE2)	3.14 pu

Table 4.5 Hydro turbine parameters

Parameter	Value	Parameter	Value
Water starting time (T_W)	2.0 s	Head at rated condition	1.0 pu
Penstock head loss co-efficient (f_p)	0.02 pu	Output power at rated condition	1.0 pu
Turbine damping constant (D)	0.5 pu	Gate position at rated conditions	1.0 pu
Initial operating head	1.0 pu	Rated no-load flow	0.05 pu

Table 4.6 Hydro governor parameters

Parameter	Value	Parameter	Value
Governor model	Gov 1	Pilot valve and servomotor time constant (T_p)	0.05 s
Permanent droop (R_p)	0.03 pu	Servo gain (Q)	5.0 pu
Temporary droop (R_t)	0.40 pu	Main servo time constant (T_g)	0.2 s
Dead band value	0.0 pu	Reset or dashpot time constant (T_R)	5.0 s
Maximum gate position (Gmax)	1.0 pu	Maximum gate opening rate (MXGTOR)	0.16 pu/s
Minimum gate position (Gmin)	0.0 pu	Maximum gate closing rate (MXGTCR)	0.16 pu/s

The SM dynamic responses were observed by the simulated test system in PSCAD/EMTDC with a simulation time step of 50 μs. The simulated results obtained for the 0.1 pu constant P load addition is given in Figure 4.5. Figures 4.5(a) and (b) show that the coupling effect between the active power and the reactive power causes transients in the responses of both. However, Figure 4.5(a) depicts that the active power output from the synchronous machine has experienced a step increment of 0.1 pu and has reached the new steady state relatively faster than the reactive power. The low-frequency oscillations observed in the reactive power response as well as the other variables given in Figure 4.4 could possibly be due to the most commonly occurring low-frequency oscillations in hydro dominant systems. The non-linearities associated with the slow-acting hydro governor have an impact on those frequency oscillations [40].

As can be explained via the swing equation, the sudden electrical power demand has slowed down the speed of the rotor. This has been verified by the rotor speed measurement (Figure 4.5(d)) and the system frequency measurement obtained via the PLL (Figure 4.5(e)). The amount of initial dip in the rotor speed is influenced by the inertia constant of the machine, while damping co-efficient of the machine influences the settling time.

The absence of the secondary frequency controller has caused a steady state error in the new system frequency. The amount of steady state frequency deviation is governed by the set *f*-droop characteristic. Therefore, new steady state frequency deviation can be calculated for an active power deviation (ΔP) of 0.1 pu and frequency droop co-efficient (D_f) of 0.03 pu as;

$$\frac{\Delta f}{\Delta P} = D_{\mathrm{f}}$$

$$\Delta f = 0.003 \text{ pu}$$

The expected new steady state frequency value (1-0.003 = 0.997 pu) exactly matches the simulated results for the external frequency measurement (Figure 4.5(e)) and the internal speed measurement (Figure 4.5(d)). The governor throttle valves have been widened more (Figure 4.5(c)) to allow a larger water flow to the prime mover so that a higher mechanical torque is created to supply more mechanical power to the generator. The steady state mechanical power increment is 0.1 pu (Figure 4.5(f)), which is equal to the additional active power requirement.

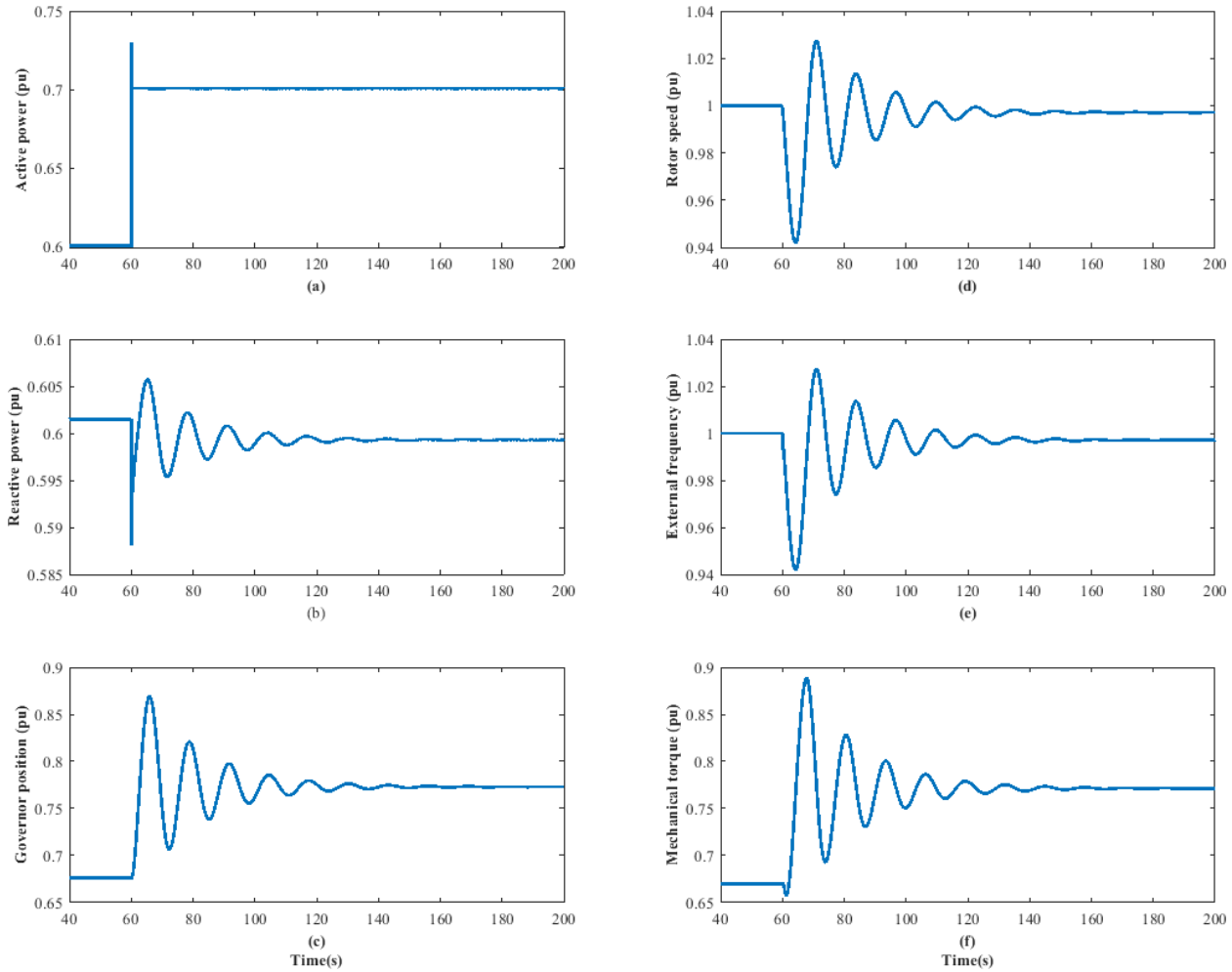

Figure 4.5 SM's (a) active power supply at PCC, (b) reactive power supply at PCC, (c) governor valve position, (d) rotor speed, (e) external frequency from PLL, (f) mechanical torque variation following the 0.1 pu constant P load addition.

The additional reactive power demand is less than 0.1 pu, for the 0.1 pu of inductive load addition (Figure 4.6(b)). This is due to the constant impedance nature of those inductive loads. The coupling effect between active power generation and reactive power generation creates some transients in active power supply from SM (Figure 4.6(a)). More reactive current is drawn to meet the additional reactive power demand. This is verified via the increment of the rms value (Figure 4.6(c)) and the increment of the lag-phase angle of the load current.

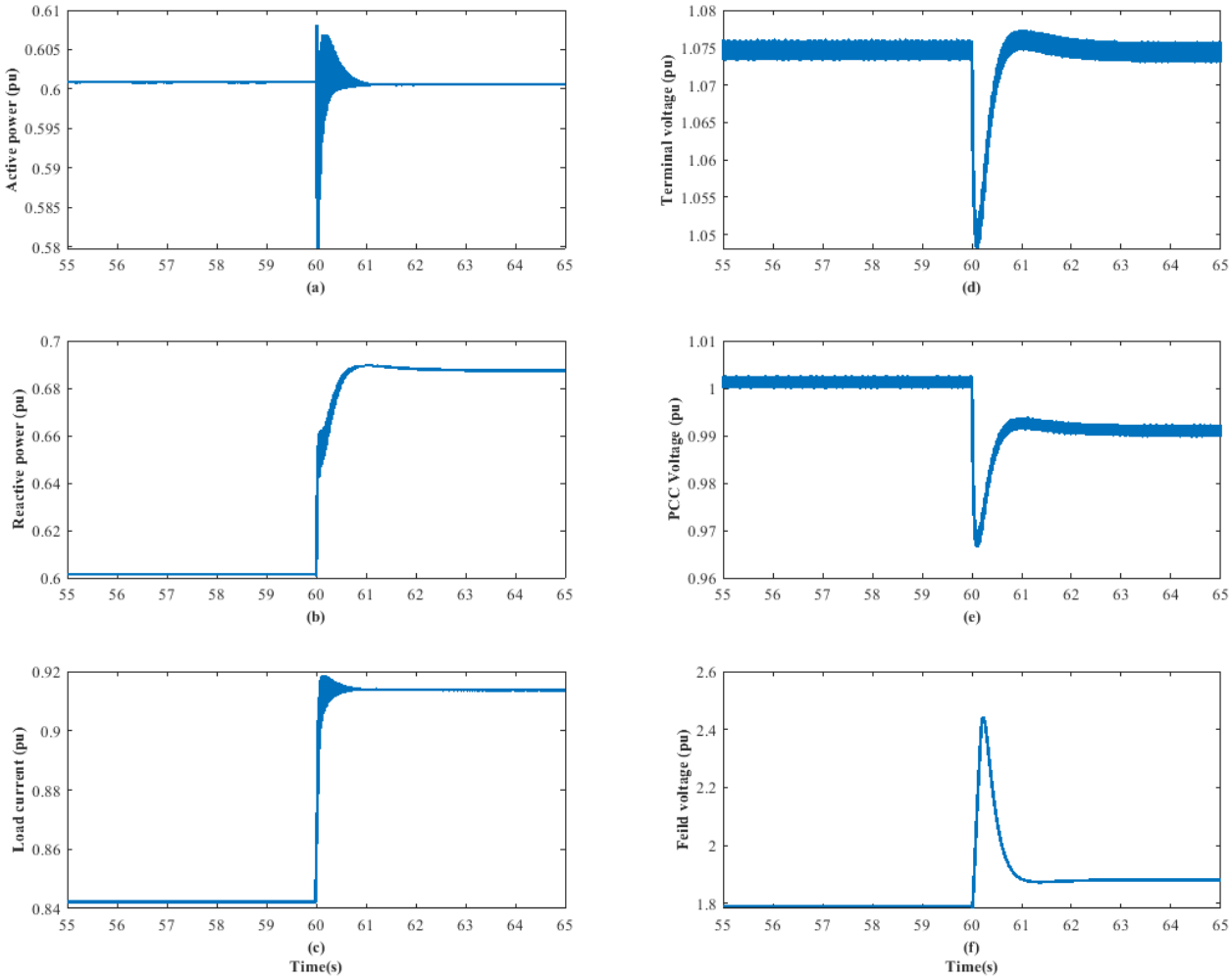

Figure 4.6 SM's (a) active power output, (b), reactive power output, (c) load current, (d) terminal voltage, (e) voltage at PCC, (f) field voltage variation for the 0.1 pu constant L load addition

The exciter has increased the field voltage (Figure 4.6(f)) and in return the field current to maintain the machine terminal voltage. The field action restores the machine's terminal voltage as given by Figure 4.6(d). The voltage drop between the SM and the PCC rises with more reactive

current flowing out (Figure 4.6(e)). The new steady state voltage at PCC is governed by the voltage (v)- current (i) relationship given by (4.5) and (4.6).

$$(v_{pcc,R}+jv_{pcc,I}) = v_{terminal}-(R+jX)*(i_R+ji_I)$$

$$v_{pcc,R} = v_{terminal} - Ri_R+Xi_I \tag{4.5}$$

$$v_{pcc,I}= -Ri_I - Xi_R \tag{4.6}$$

Real and imaginary parts of the PCC voltage ($v_{pcc,R}$, $v_{pcc,I}$) are obtained by machine terminal voltage ($v_{terminal}$), resistive (R) and inductive (X) impedance between the machine terminal and PCC, and the real and imaginary parts of the current (i_R, i_I)

The responses of SM to the three-phase-to-ground solid fault for 6 cycles (≈ 0.1s) are given in Figure 4.7. The zero-fault impedance lowers the PCC voltage down to zero (Figure 4.7(g)). Therefore, all the fault current will flow through the fault path making zero active power and zero reactive power transfers to the load as given by Figures 4.7(e) and (f), respectively.

With the drop of active power consumption by the load, the active power generation by the SM falls as well (Figure 4.7(a)). However, there is still some active power generation to compensate for the power losses in the transformer and the transmission line resistance. The inductance-dominant path between the SM terminal and PCC makes a considerable reactive power to flow. This is verified by the significantly large reactive power generation by the SM (Figure 4.7(b)). The voltage drop across the transformer and transmission line reactance causes a non-zero voltage at the SM terminal (Figure 4.7(c)). The short circuit created at the PCC reduces the impedance of the current conducting path. Therefore, current has risen to a peak of around 3.0 pu (Figure 4.7(d)). The exciter action increases the field voltage (Figure 4.7(h)) to restore the machine's terminal voltage. The increment of field voltage leads to a rise in the field current as well. The slow-acting exciter control loop causes an increment of the field voltage, even after 0.2 s of the fault clearance.

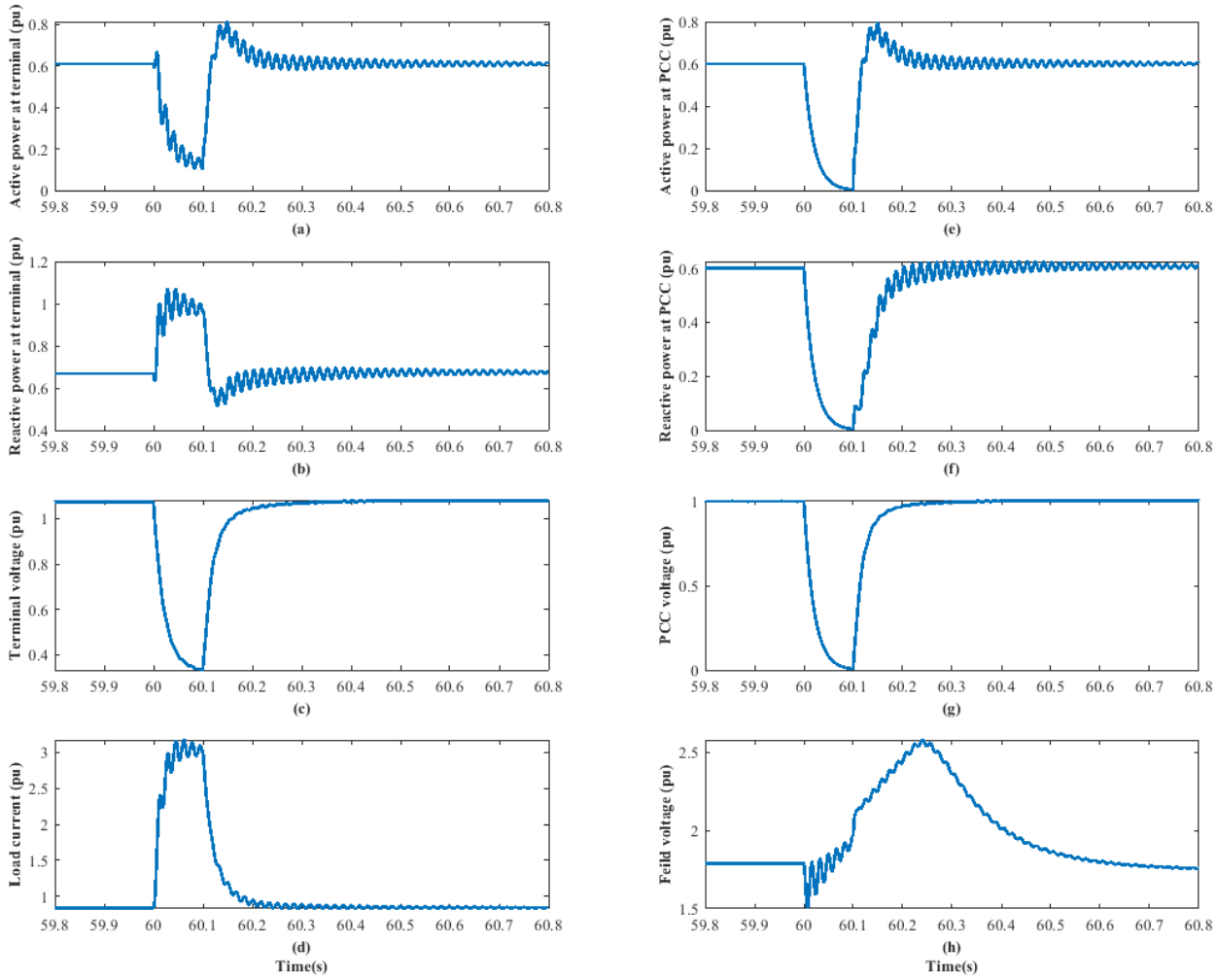

Figure 4.7 SM's (a) active power at terminal, (b) reactive power at terminal, (c) terminal voltage, (d) load current, (e) active power at PCC, (f) reactive power at PCC, (g) voltage at PCC, (h) field voltage variation for solid three phase-ground fault at PCC for 0.1 s

The slow-acting governor action has caused a negligible reduction in the mechanical power input. Therefore, with almost a constant active power input and a considerably low active power output, SM's rotor has accelerated according to the swing-equation (Figure 4.8). The SM's dynamic behaviour during the transient and sub transient periods has caused the initial reduction of the machine speed. After the fault clearance, the active power, reactive power, voltage, and

current values are restored within 0.8 s, while low-frequency oscillations appear in the rotor speed variation for a longer period of time.

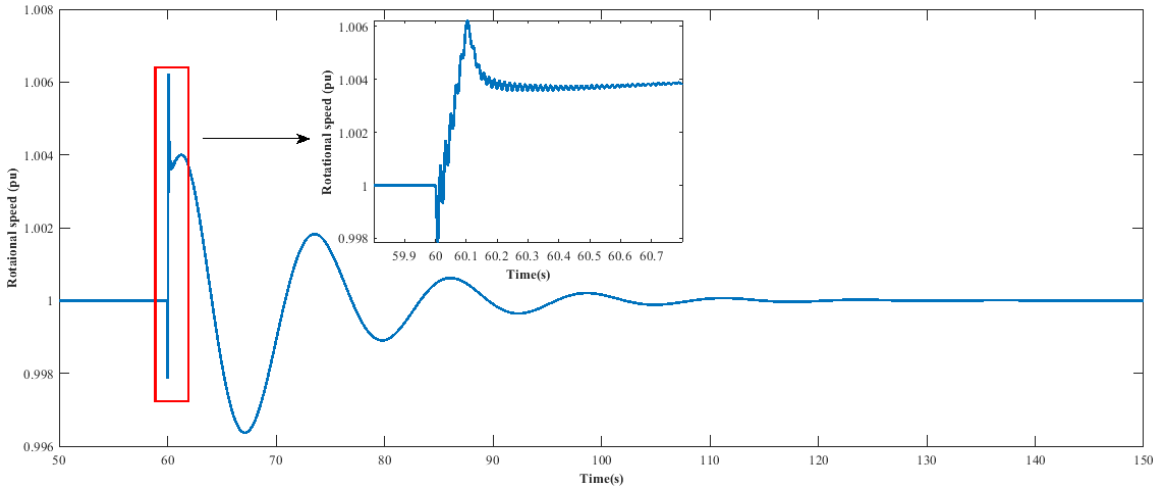

Figure 4.8 The rotational speed variation for a solid three phase-ground fault at PCC for 0.1 s

The SM's responses to a high impedance fault (HIF), which creates 0.5 pu voltage at PCC is also simulated. The fault reactance and the fault duration are set be 0.2 H and 0.1 s, respectively. Though there is not any universally accepted definition for a HIF, the HIF at distribution level has been defined as *"a high impedance ground fault results when a primary conductor makes an unwanted electrical contact with a road surface, side walk, sod, tree limb, or with other surface, or object which restricts the flow of fault current to a level below that reliably detectable by conventional over-current devices"* by the Power System Relaying Committee (PSRC) Working Group 15 [41]. The responses are similar to the solid three-phase-to-ground fault except the higher reactive power consumption by the fault reactance, lower active power reduction and lower overshoots of currents and voltages (Figure 4.9).

4.3 VSM0H Time-Domain Simulation Results

The VSM0H model is developed in PSCAD/EMTDC according to the controller architecture given in section 3.1. The rest of the test system is given in Figure 4.1. Its parameters are given in Table 4.1, and Table 4.2. VSM0H controller parameters used in the test system are given in Table 4.7. The dynamic responses against the constant P load addition, constant L load addition, solid three-phase-to-ground fault, and HIF are observed with a simulation time step of 5 μs. The THD

analysis shows a 0.82% for current and 1.10% for the voltage at PCC. According to the controller topology given in Figure 3.1, it uses the calculated *P* and *Q* values. But this simulation uses the measured *P* and *Q* at the machine terminal.

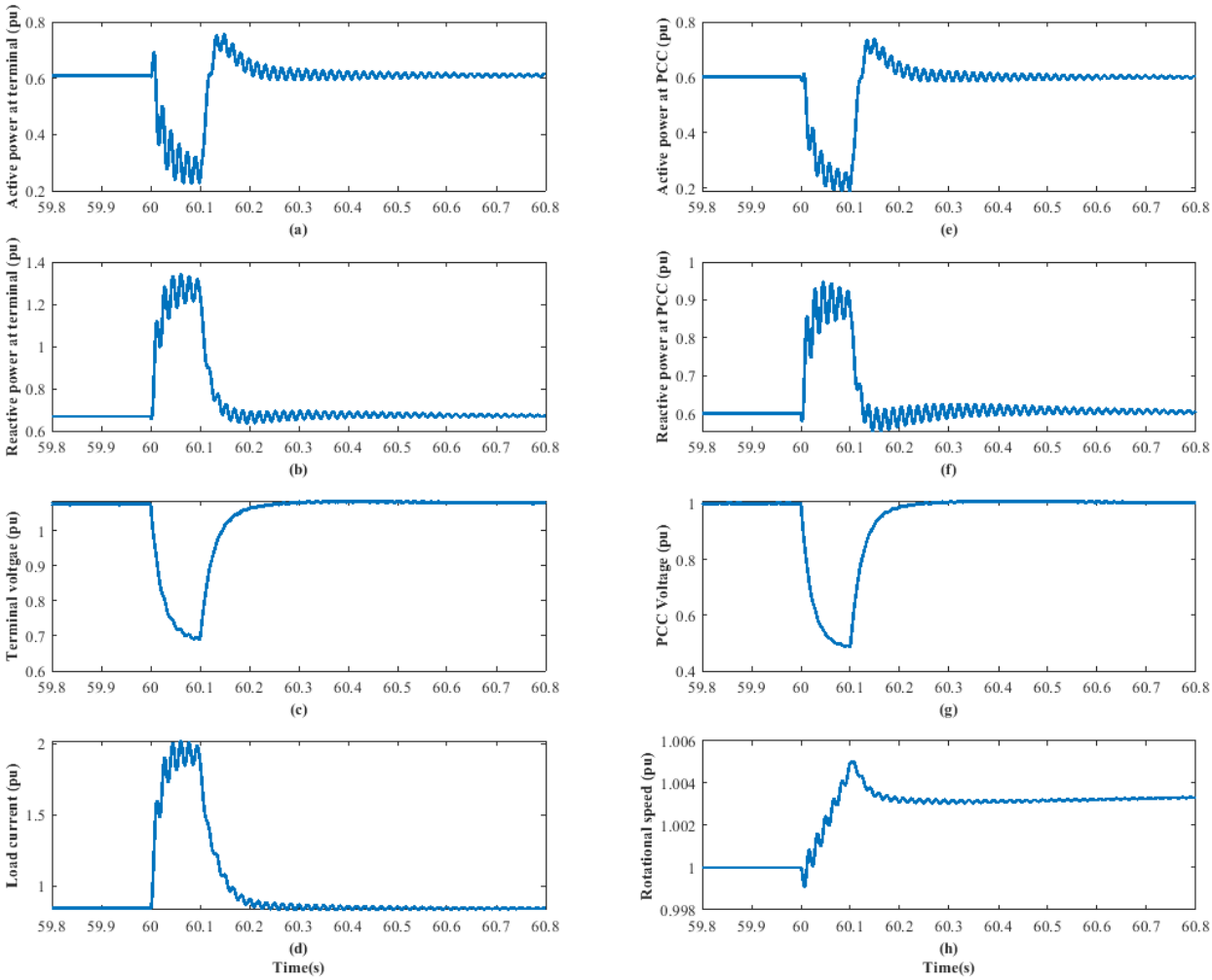

Figure 4.9 SM's (a) active power at terminal, (b) reactive power at terminal, (c) terminal voltage, (d) load current (e) active power at PCC, (f) reactive power at PCC, (g) volatage at PCC, (h) rotational speed variation for HIF three phase-ground fault at PCC for 0.1 s

Table 4.7 VSM0H controller parameters

Parameter	Value	Parameter	Value
P_{set}	0.6 pu	f_{set}	1.0 pu
Q_{set}	0.6 pu	v_{set}	1.2 pu
D_f	0.03 pu	D_v	0.03 pu
f_0	60 Hz	Low-pass filter's time constant	0.01667 s

The simulated results obtained for the 0.1 pu of constant P load addition and constant L load addition are given in Figure 4.10 and Figure 4.11, respectively. The 0.1 pu constant P load addition increses the active power supply exactly by 0.1 pu (Figure 4.10(a)). The VMS0H model does not facilitate complete decoupled control of active power and reactive power. Therefore, reactive power also undergoes some transients (Figure 4.10(b)). The required additional active power is taken from the proper modulation of the power coming from the dc side (Figure 4.10(e)). The dc power input increment is exactly equal to 0.1 pu.

The system frequency measurement (via a PLL) contains high-frequency noise due to the converter's switching action (Figure 4.10(d)). The average value of system frequency measurement and the calculated virtual rotor speed (Figure 4.10(c)) show a similar behaviour. The fast-acting VSM0H model results in a better frequency nadir of 0.994 pu than the inertial support included SM case that was equal to 0.942 pu. Therefore, apart from the higher order harmonics genertaion, the power electronic converters can be propoerly manipulted to obtain the advantage of its fast-acting capability for grid frequncy support. As explained in section 3.1, for a given frequency droop co-efficient, the time constant of the low-pass filter is proportional to the intertia time constant. Therefore, by minimizing the low-pass filter's bandwidth, i.e., by increasing fiter's time constant, more inertial support can be emulated to reduce the frequency nadir. The simulated results for several filter bandwidth are given in Figure 4.12. The primary frequency control action results in a steady state frequency deviation. As explained in section 4.2, a similar calculation can be done to verify the match between the calculated and the simiulated frequency speed deviations. Figure 4.12 further illustrates that the time constant of the low-pass filter could impact only in the transient response and as long as the frequency droop co-efficient is a constant the frequency will settle at the same level.

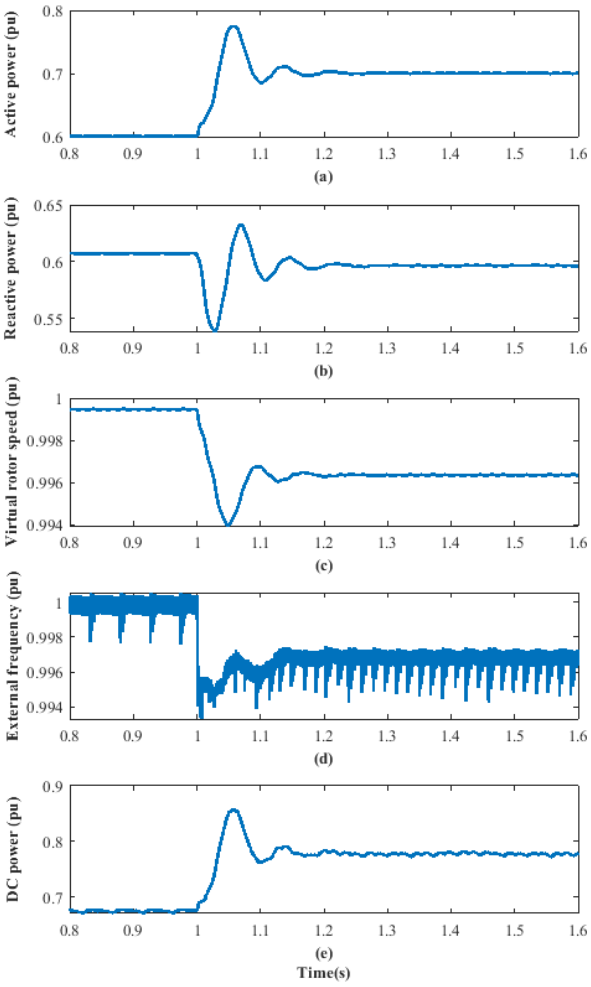

Figure 4.10 VSM0H model's (a) active power at PCC, (b) reactive power at PCC, (c) virtual rotor speed, (d) system frequency (PLL), (e) dc power variation following the 0.1 pu constant P load addition

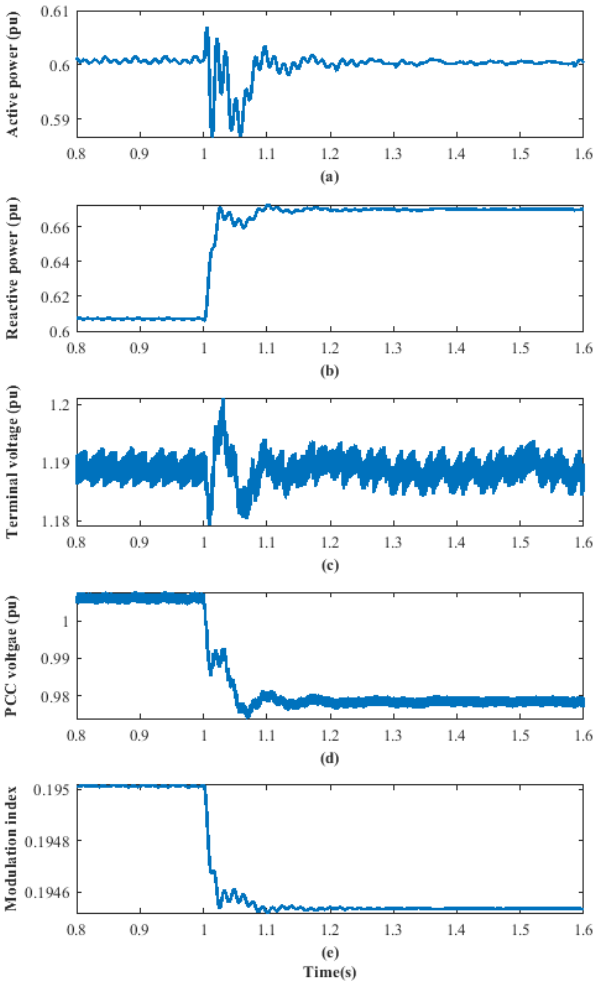

Figure 4.11 VSM0H model's (a) active power at PCC, (b) reactive power at PCC, (c) VSM terminal voltage, (d) voltage at PCC, (e) modulation index variation following the 0.1 pu of constant L load addition

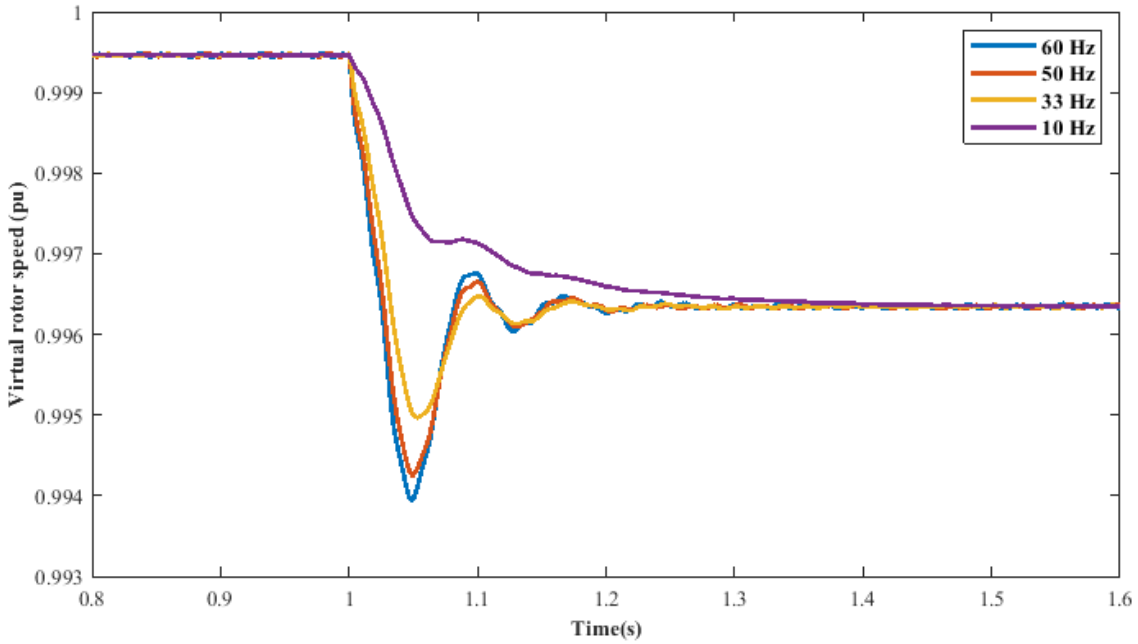

Figure 4.12 The impact on frequency nadir from different low pass filter band widths

The increment of reactive power supply to the for 0.1 pu of inductive load addition is less than 0.1 pu (Figure 4.11(b)), due to the constant impedance nature of the load. The prevailing coupling effect causes transients in the active power supply (Figure 4.11(a)). The in-built *Q*-*v* control action of the VSM0H model govenrs the converter terminal voltage. For the resaultant 0.1 pu of reactive power difference at the converter terminal and with a 0.03 pu of *Q*-*v* droop co-efficient, the expected terminal volatge variation is 0.003 pu, which is too small to oberve in Figure 4.11(c). More reactive current has been drawn to meet the additional reactive power requirement, which can be verified by the increment of the rms value of the load current and the increment of the lagging phase angle. The larger reactive current creates a larger voltage drop across the converter terminal and the PCC. The *v*-*i* caharacteristic, which depends on the transformer and line impedance together with the *Q*-*v* characteristic set the PCC voltage (Figure 4.11(d)). Both of these charcteristics determine the reactive power sharing in parallel-connected VSM0H-based converters.

The VSM0H model does not emulate the field action, which restores the converter terminal voltage. The *Q*-*v* control loop of the VSM0H model generates the VSM terminal volatge, which will then be appropriately scale down using the dc volatge to obtain the modulation index of the refence signal to be used for PWM switching action. Figure 4.11(e) shows that the modulation

index has reduced to follow the *Q*-*v* characteristic rather trying to restore the terminal voltage of the VSM. This avoids optimal emulation of exciter operation by the VSM0H model. Simualtion results further reveal the absence of the dc power modulation in supporting the reactive power demand.

VSM0H has been tested for a solid three-phase-to-ground fault at the PCC for a period of 0.1 s and for a HIF at the PCC for a period of 0.1 s; the latter creates 0.5 pu of voltage drop at the PCC. Simulation results for the respective cases are given in Figures 4.13 and 4.14. The required HIF level is obtained by using a fault reactance of 0.15 H.

Three-phase-to-ground solid fault sets the bus volatge to zero (Figure 4.13(g)). As all the fault current passes through the faulted path, the active and reactive power transfer to load during the fault drop to zero (Figure 4.13(e) and Figure 4.13(f)). Similar to a SM, in VSM0H model the active power generation of the converter drops to a level to only compensate for the power losses across the transformer and transmission line's resistive parts (Figure 4.13(a)). The inductive dominant path created by the transfomer's leakage reactance and the transmission line's effective inductance draw more reactive power (Figure 4.13(b)). The voltage drop between the converter terminal and the PCC determines the VSM's terminal volatge (Figure 4.13(c)).

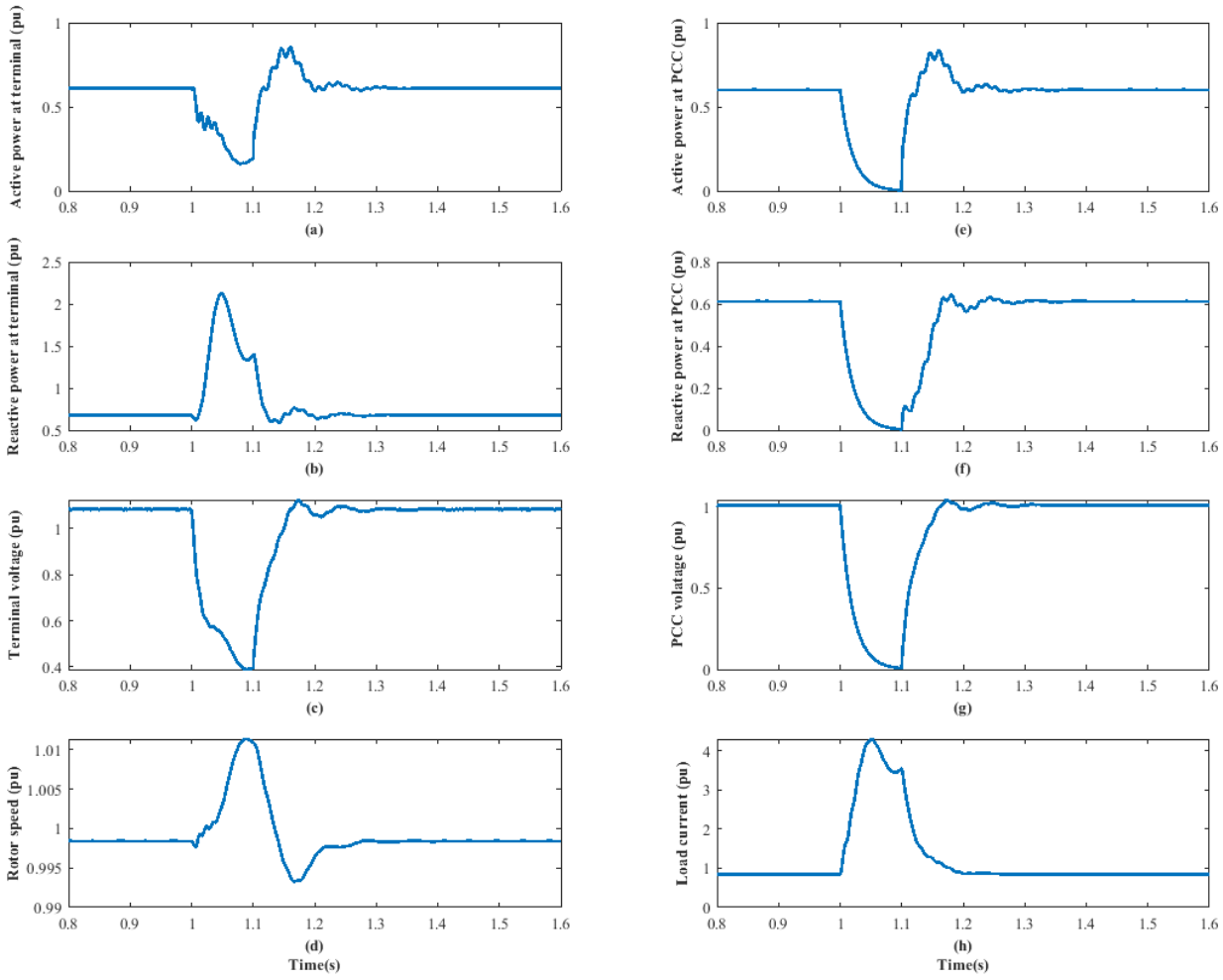

Figure 4.13 VSM0H model's (a) active power at VSM terminal, (b) reactive power at VSM terminal, (c) VSM terminal voltage, (d) VSM virtual rotor speed, (e) active power at PCC, (f) reactive power at PCC, (g) volatage at PCC, (h) load current variation for solid three phase-ground fault at PCC for 0.1 s

The fault currrent level reaches a peak of 4.3 pu, in contrast to the 3.0 pu peak current of the SM (Figure 4.13(h)). The virtual rotor of the VSM0H model accelerates similarly to the rotor response of SM. However, the virtual rotor of the VSM0H model reaches a peak value of 1.011 pu (Figure 4.13(d)) as opposed to the 1.006 pu peak value of the SM. The virtual rotor accelerates to a much higher value as it does not have an explicit inertia emulation loop. The time taken for restoration after the fault clearance is around 0.2 s, which is faster than the 80 s in the SM case.

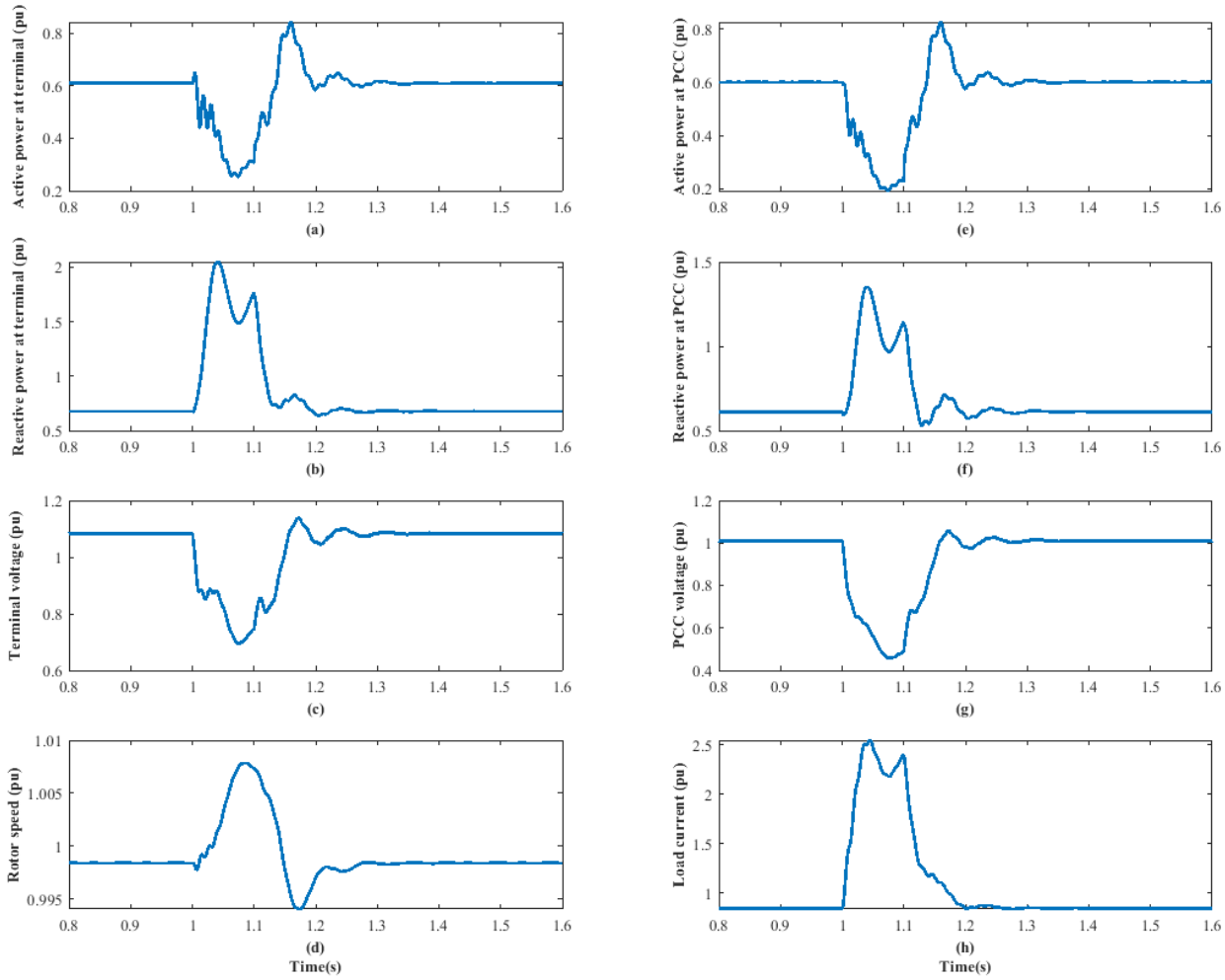

Figure 4.14 VSM0H model's (a) active power at VSM terminal, (b) reactive power at VSM terminal, (c) VSM terminal voltage, (d) VSM virtual rotor speed, (e) active power at PCC, (f) reactive power at PCC, (g) voltage at PCC, (h) load current variation for high impedance three phase-ground fault at PCC for 0.1 s

The response of the VSM0H model to the HIF can be explained similarly to the solid three-phase-to-ground fault. The fault reactance consumes a larger amount of reactive power due to the inductive fault impedance (Figure 4.14(f)). The fault impedance curtails the fault current's rise to be around 2.5 pu (Figure 4.14(h)). As the loss of active power is lower (Figures 4.14(a) and (e)) than the solid three-phase-to-ground fault, the peak speed of the virtual rotor could reach only around 1.0078 pu. The VSM0H's response to HIF is comparable to the same level of HIF with SM.

4.4 VC-VSC Time-Domain Simulation Results

The algorithm explained in section 3.2 is used to control the converter of the test system given in Figure 4.1. The parameters of the test system are the same as in Tables 4.1 and 4.2. The VC-VSC has also been tested under the aforementioned four tests in PSCAD/EMTDC using a simulation time step of 5 μs. The THD at PCC for voltage and current are 1.1% and 0.8%, respectively, which indicate a robust power quality level at the PCC. The VC-VSC controller parameters are given in Table 4.8. The simulation results obtained for the 0.1 pu constant P load addition and 0.1 pu constant L load addition are given in Figures 4.15 and 4.16, respectively.

Table 4.8 VC-VSC controller parameters

Parameter	Value	Parameter	Value
P_{set}	0.6 pu	f_{set}	1.0 pu
Q_{set}	0.6 pu	v_{set}	1.2 pu
D_f	0.03 pu	D_v	0.03 pu
H	3 s	K_D	20 pu

For the 0.1 pu of constant P load addition, output active power, output reactive power, and the input dc power variations (Figure 4.15(a),(b), and (e)) can be explained similarly to the VSM0H model. Compared to the VSM0H model, the VC-VSC has the swing equation-based inner controller in the *P-f* control path. This swing equation-based path influences only the transient responses. The steady state responses can be explicitly explained using the frequency droop relationship. The emulated rotor with an inertia time constant of 3 s has slowed down the speed variations and has resulted in a sluggish frequency response (Figures 4.15(c)-(d)) compared to the VSM0H model. The virtual rotor of VC-VSC has taken 1 s to reach the new steady state compared to the 0.2 s in the VSM0H model. The VC-VSC shows a better frequency recovery than a conventional SM. The frequency response can be smoothed out by controlling the inertia time constant. The frequency responses for arbitrarily selected inertia time constants following the same resistive load addition are given in Figure 4.17. This clearly shows the ability of the VSMs with higher inertia to have a smoother frequency recovery, but with a longer settling time. Higher inertia requires higher dc side energy support. Therefore, control parameters must be selected under these limitations.

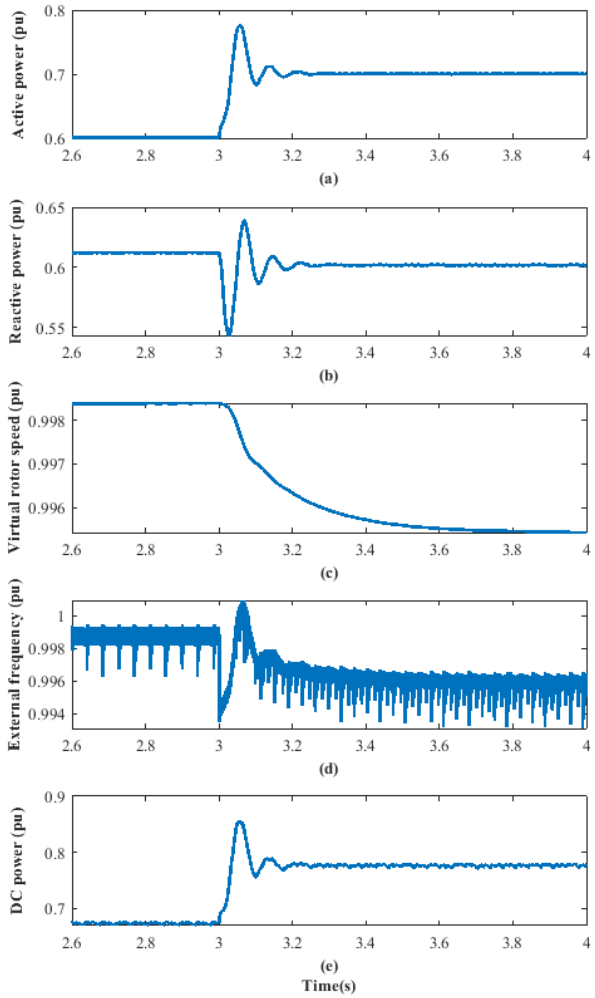

Figure 4.15 VC-VSC model's (a) active power at PCC, (b) reactive power at PCC, (c) virtual rotor speed, (d) system frequency (PLL), (e) dc power variation following the 0.1 pu constant P load addition

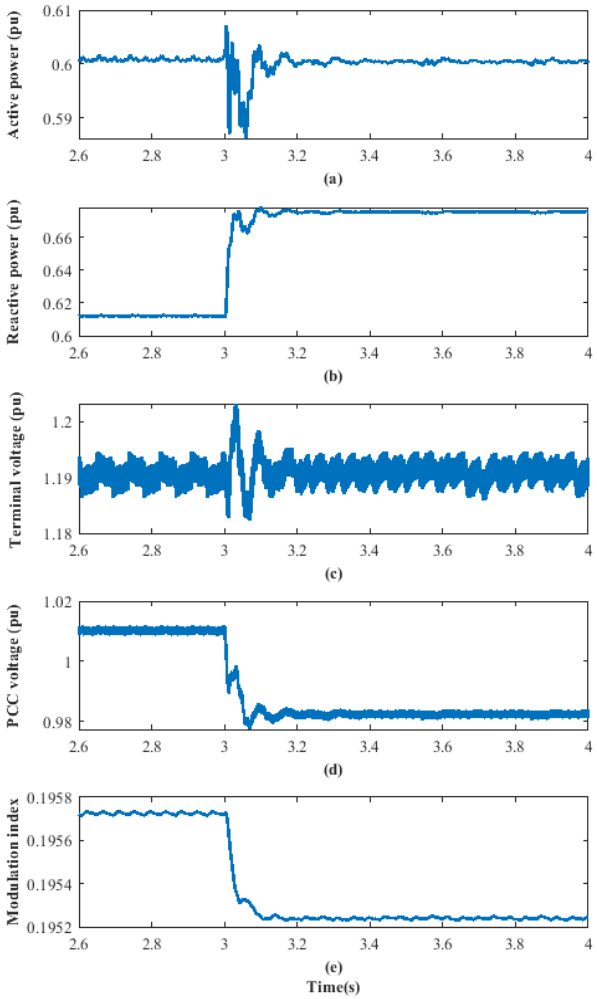

Figure 4.16 VC-VSC model's (a) active power at PCC, (b) reactive power at PCC, (c) VSM terminal voltage, (d) voltage at PCC, (e) modulation index variation following the 0.1 pu of constant L load addition

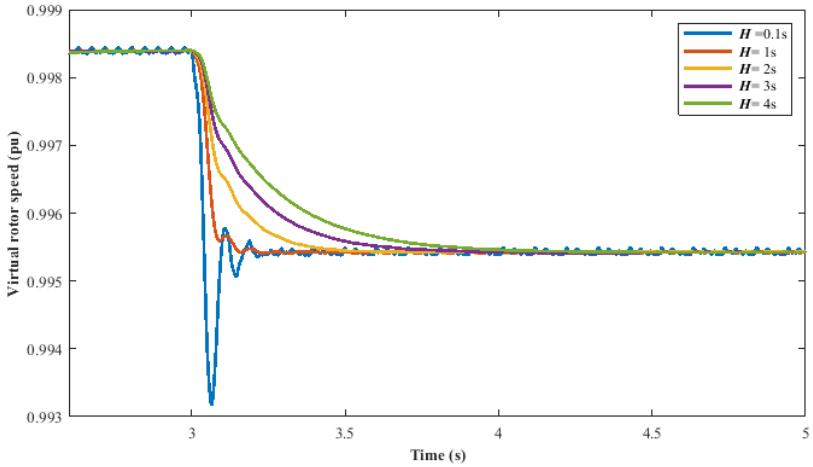

Figure 4.17 Impact of inertia time constant in frequency response

As the *Q-v* controller is same for both VSM0H and VC-VSC, their responses following a 0.1 pu of constant L load addition are similar and can be explained similarly. Figure 4.18 depicts the VC-VSC's response to a solid three-phase-to-ground fault at the PCC for 0.1 s (6 cycles). The variations of active power, reactive power, and the voltage at the converter terminal (Figures 4.18(a)-(c)) and the variations of active power, reactive power, and the voltage at the PCC (Figures 4.18 (e)-(g)) are similar to those of the VSM0H and can be explained similarly. The VC-VSC has also resulted in a 4.3 pu peak fault current level, similar to the VSM0H model. The slow-acting inertia emulating path has limited the rotor's acceleration to around 1.0023 pu, which is much lower than the VSM0H model. Compared to the SM with the same level of inertia, the peak rotor

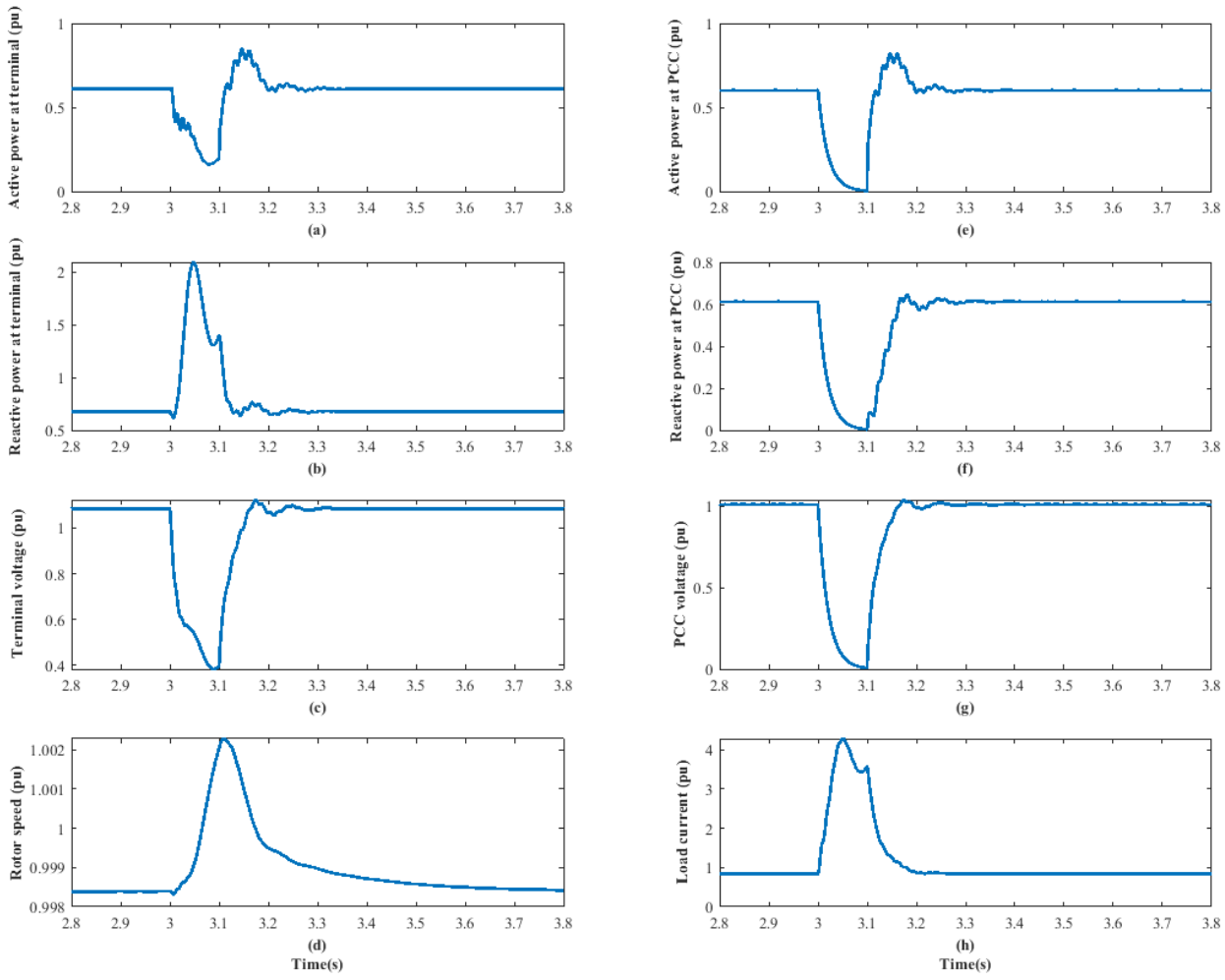

Figure 4.18 VC-VSC model's (a) active power at VSM terminal, (b) reactive power at VSM terminal, (c) VSM terminal voltage, (d) VSM virtual rotor speed, (e) active power at PCC (f) reactive power at PCC, (g) volatage at PCC, (h) load current variation for solid three phase-ground fault at PCC for 0.1 s

speed following the disturbance is lower in the VC-VSC. This is due to the fast-acting capability of converters compared to the electro-mechanical circuitry of SMs. The responses of the VC-VSC to a HIF, which creates a 0.5 pu terminal voltage reduction, is tested for 0.1 s and the obtained results are given in Figure 4.19. The responses are comparable to the VSM0H model's responses to the same level of HIF. The blocking of rotational speed overshoot by the emulated inertia can be seen in this case as well.

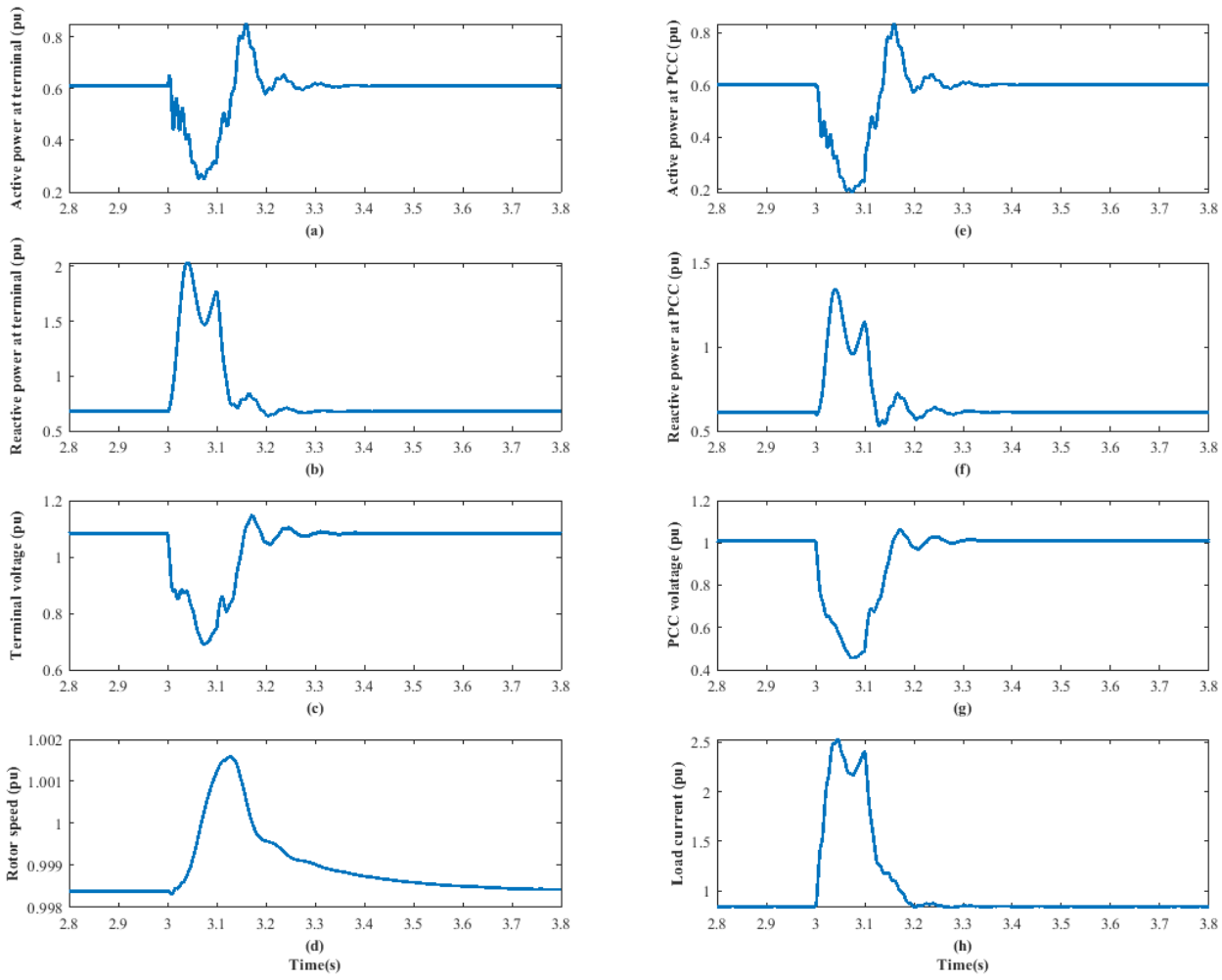

Figure 4.19 VC-VSC model's (a) active power at VSM terminal, (b) reactive power at VSM terminal, (c) VSM terminal voltage, (d) VSM virtual rotor speed, (e) active power at PCC, (f) reactive power at PCC, (g) voltage at PCC, (h) load current variation for high impedance three phase-ground fault at PCC for 0.1 s

4.5 Modified-VSM0H Time-Domain Simulation Results

The test system given in Figure 4.1 is controlled using the modified VSM0H model given in section 3.3. The simulations are carried out with a 5 μs simulation time step in PSCAD/EMTDC. The parameters of the test system are listed in Tables 4.1 and 4.2. The modified VSM0H controller's parameters are given in Table 4.9. K_{Pf}, T_{If}, K_{Pv} and T_{Iv} represent the proportional gain and integrator time constant of the PI controller of *P-f* controller and proportional gain and integrator time constant of the PI controller of *Q-v* controller, respectively. All other parameters are explained in section 3.3. The THD levels of current and voltage at the PCC are 0.85% and 1.2%, respectively.

Table 4.9 Modified VSM0H controller parameters

Parameter	Value	Parameter	Value
P_{set}	0.6 pu	f_{set}	1.0 pu
Q_{set}	0.6 pu	v_{set}	1.2 pu
D_f	0.03 pu	D_v	0.03 pu
H	3 s	K_D	20 pu
K_{Pf}	1.0 pu	K_{Pv}	1.0 pu
T_{If}	0.1 s	T_{Iv}	1.2 s

The simulation results obtained for the 0.1 pu constant P load addition and 0.1 pu constant L load addition are given in Figures 4.20 and 4.21, respectively.

Compared to the VC-VSC, the modified VSM0H model has a PI controller-based *P-f* droop controller path to emulate the governor signal. This sluggish external controller path has slowed down the entire frequency response of the system more than the previously stated two VSM algorithms. Figures 4.20(c) and (d) verify this with a frequency settling time of 8 s for a 0.1 pu constant P load addition. The active power output (Figure 4.20(a)), reactive power output (Figure 4.20(b)), and the dc power input (Figure 4.20(e)) variations can be described similarly to the VC-VSC.

Responses of the modified VSM0H to a constant L load addition (Figure 4.21) can be explained similarly to the VC-VSC model. The PI controller of the *Q-v* controller ensures a strict following

of the set *Q-v* droop characteristic compared to VSM0H and VC-VSC models, which also use *Q-v* droop characteristics.

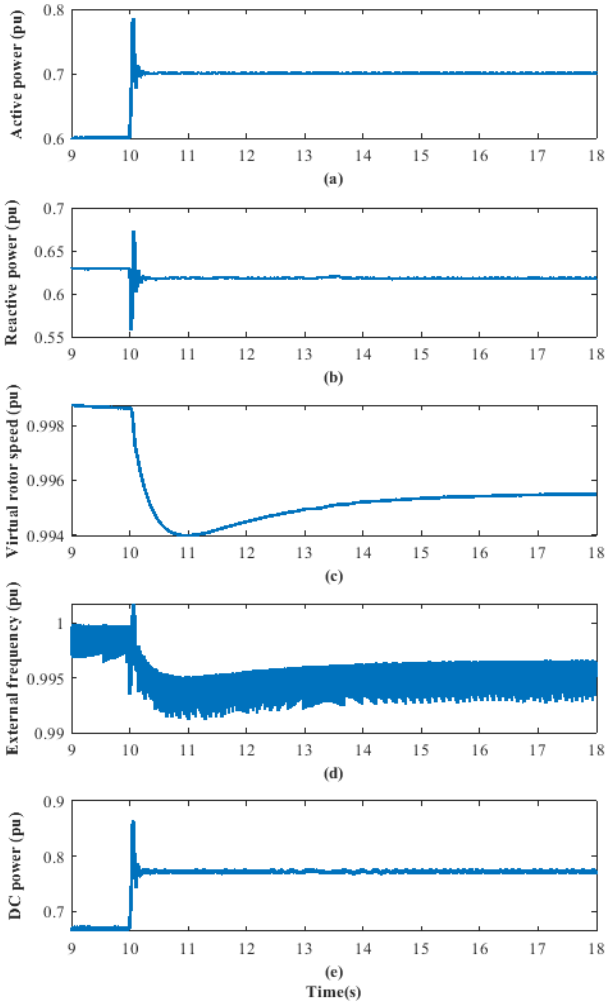

Figure 4.20 Modified VSM0H model's (a) active power at PCC, (b) reactive power at PCC, (c) virtual rotor speed, (d) system frequency (PLL), (e) dc power variation following the 0.1 pu constant P load addition

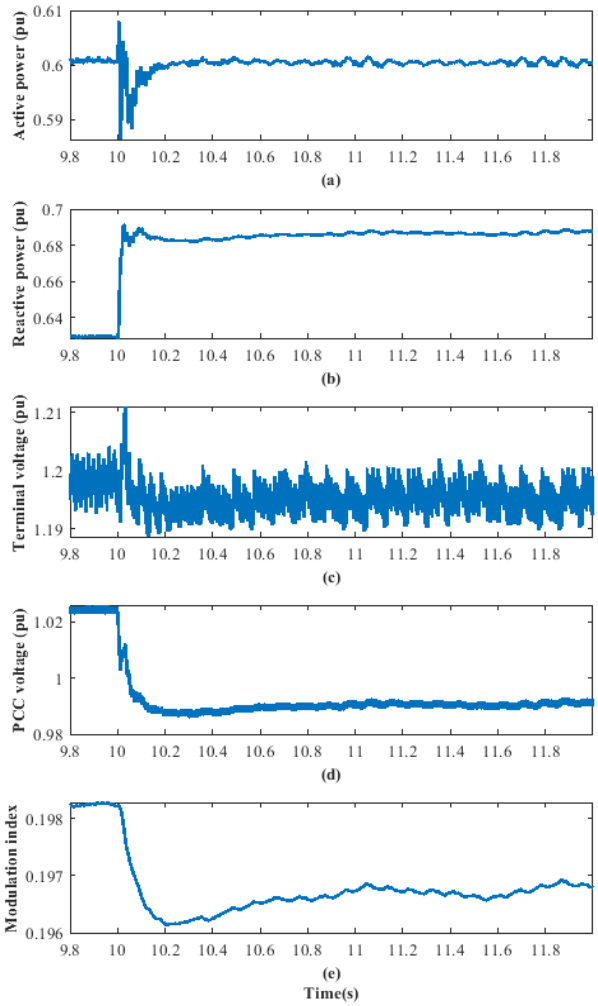

Figure 4.21 Modified VSM0H model's (a) active power at PCC, (b) reactive power at PCC, (c) VSM terminal voltage, (d) voltage at PCC, (e) modulation index variation following the 0.1 pu of constant L load addition

Similar to the VC-VSC model, the modified VSM0H model can also emulate different levels of frequency support with different inertia time constants. Some inertia time constants may lead to instability, due to the interactions between control loops. It can be shown as given in Figure 4.22 that the reduction of inertia time constant, increment of damping co-efficient and, the reduction of the PI controller time constant can be used to speed up the modified VSM0H model's frequency response. Therefore, it can be stated that the higher inertia is always not a better option as it requires

much longer settling time. Therefore, by proper selection of control parameters a robust controller performance can be obtained.

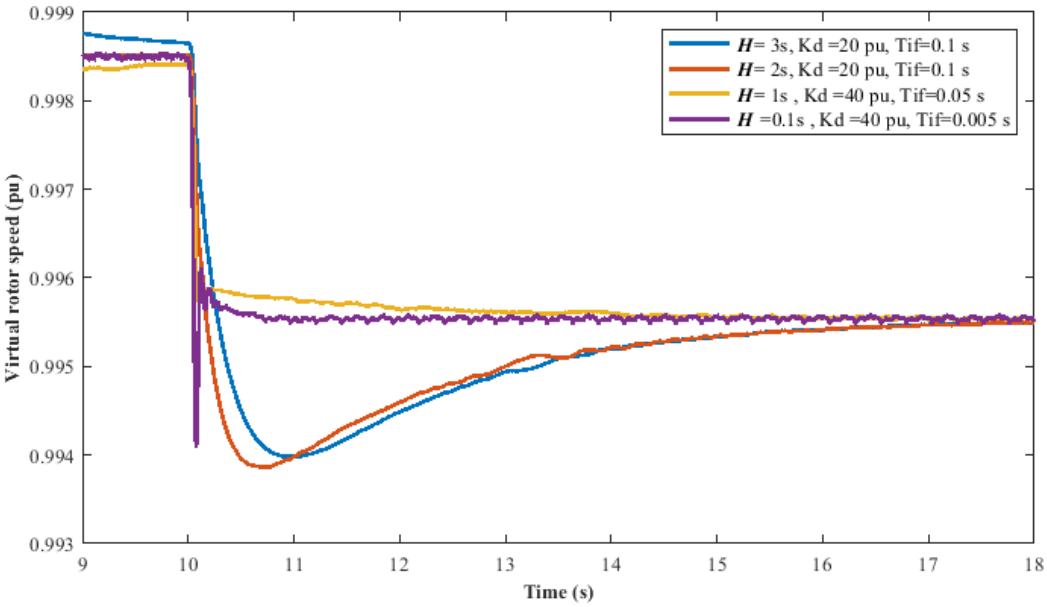

Figure 4.22 Impact of different inertia time constants, damping co-efficient and integral time constant of the PI controller on the frequency response.

The responses of the modified VSM0H model to a solid three-phase-to-ground fault are given in Figure 4.23. These responses can be explained similarly to the previously mentioned VSM algorithms. The peak value of the rotational speed subsequent to the fault is less than that of the VSM0H due to the emulated inertia; however, it is higher than the VC-VSC, as it has a sluggish PI controller.

As long as the PI controller of the *Q-v* controller has a longer time constant than the PI controller of the *P-f* controller, the overall controller will be stable. However, controllers with higher bandwidth, i.e., with faster responses, can create unacceptably large overshoots. Therefore, the modified VSM0H model requires special attention to avoid control loop interactions.

The responses obtained for the HIF level of 0.5 pu voltage at PCC are given in Figure 4.24. A fault reactance of 0.15 H and fault duration of 0.1s have been used. The modified VSM0H model's behaviour can be explained similarly to the previous two VSM algorithms.

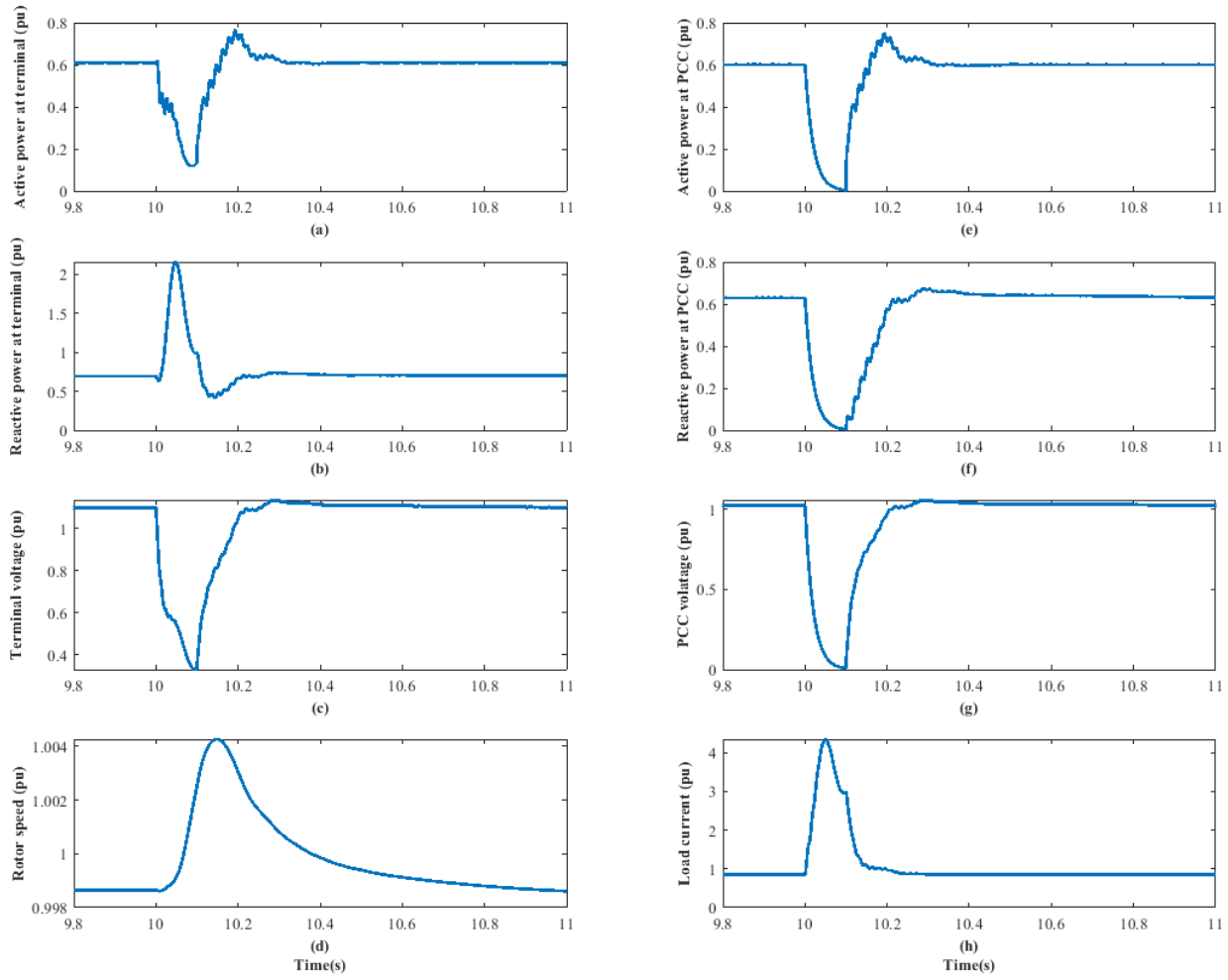

Figure 4.23 Modified VSM0H model's (a) active power at VSM terminal, (b) reactive power at VSM terminal, (c) VSM terminal voltage, (d) VSM virtual rotor speed, (e) active power at PCC (f) reactive power at PCC, (g) volatage at PCC, (h) load current variation for solid three phase-ground fault at PCC for 0.1 s

4.6 Synchronverter Time-Domain Simulation Results

The VSM algorithm explained in section 3.4 is used to control the converter given in Figure 4.1. The simulations are completed in PSCAD/EMTDC with a simulation time step 5 μs. While parameters of the test system are given in Table 4.1 and Table 4.2, the parameters of the synchronverter VSM algorithm are given in Table 4.10. According to the controller topology given in Figure 3.6, it uses the calculated *P* and *Q* values. But this simulation uses the measured *P* and *Q* at the machine terminal. The same LCL filter could reduce the THD levels of current and voltage at PCC to 1% and 1.14%, respectively.

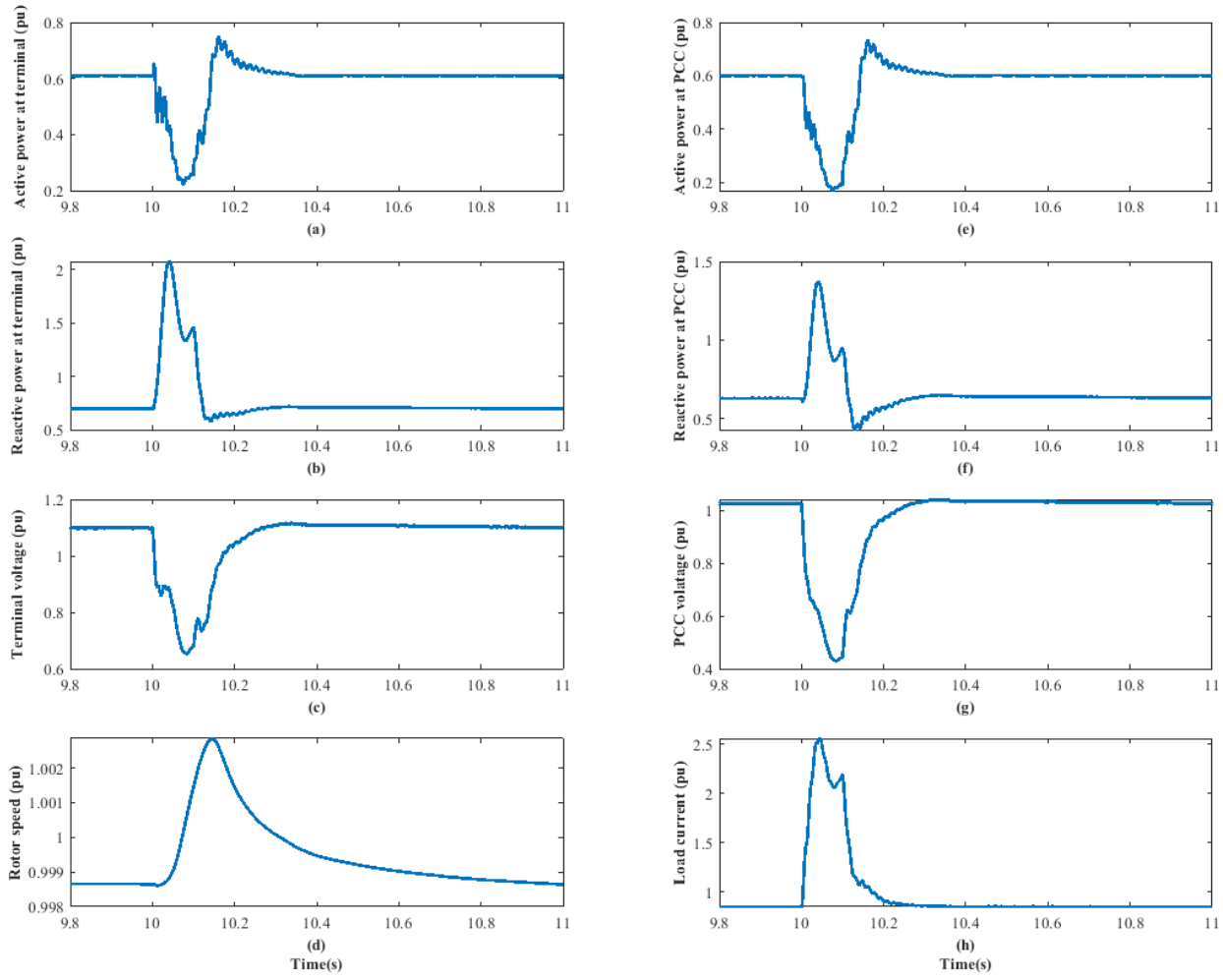

Figure 4.24 Modified VSM0H model's (a) active power at VSM terminal, (b) reactive power at VSM terminal, (c) VSM terminal voltage, (d) VSM virtual rotor speed, (e) active power at PCC, (f) reactive power at PCC, (g) voltage at PCC, (h) load current variation for high impedance three phase-ground fault at PCC for 0.1 s

Table 4.10 Synchronverter controller parameters

Parameter	Value	Parameter	Value
P_{set}	0.6 pu	$\overline{\omega_n}$	1.0 pu
Q_{set}	0.6 pu	v_{set}	1.2 pu
D_f	0.03 pu	D_v	0.03 pu
H	3 s	K	3.33 s

The active power-frequency response of the synchronverter model is close to the VC-VSC model. The absence of the damping path of the VC-VSC model in the grid-forming scenario and

the usage of damping path to emulate the drooping effect in synchronverter model have made those controllers' frequency response the same. Therefore, synchronverter's response to 0.1 pu constant P load addition (Figure 4.25) can be explained similarly to the VC-VSC. This is verified by the same frequency nadir of 0.995 pu and frequency settling time of 1s (Figure 4.25(c)).

Synchronverter's *Q-v* control loop utilizes the *Q-v* droop control together with an integral control, whereas the modified VSM0H model had used a PI controller with the *Q-v* droop controller. Therefore, synchronverter's response to the 0.1 pu constant L load addition (Figure 4.26) can be explained similarly to the modified VSM0H model.

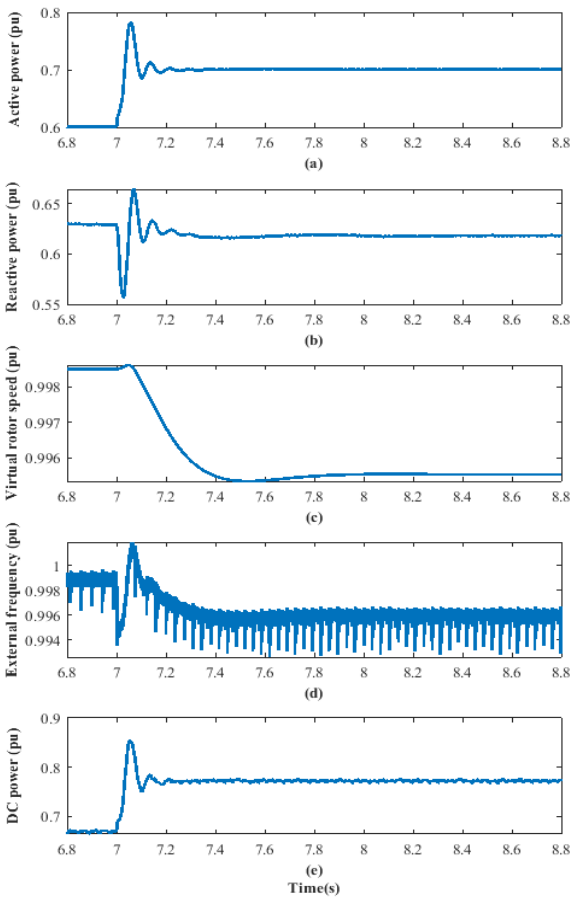

Figure 4.25 Synchronverter model's (a) active power at PCC, (b) reactive power at PCC, (c) virtual rotor speed, (d) system frequency (PLL), (e) dc power variation following the 0.1 pu constant P load addition

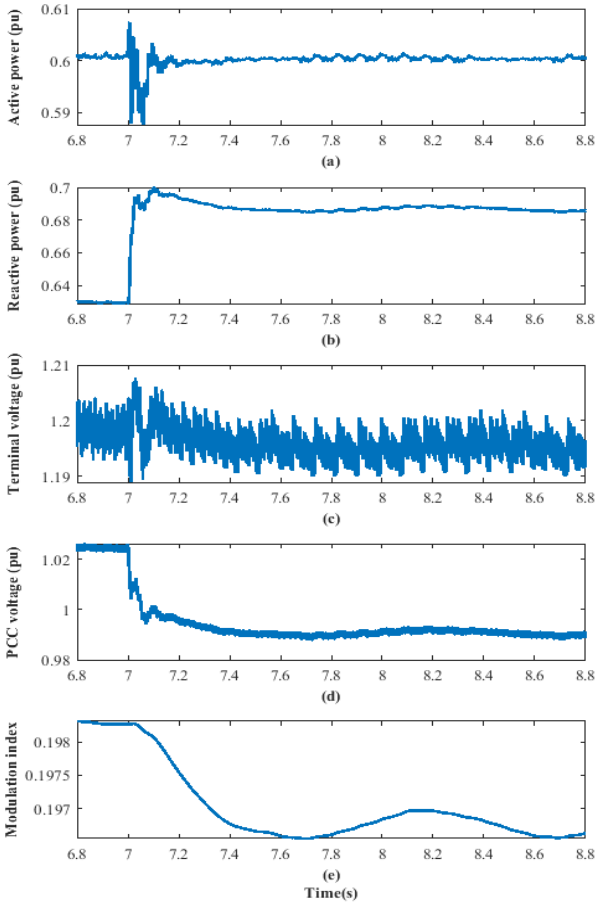

Figure 4.26 Synchronverter model's (a) active power at PCC, (b) reactive power at PCC, (c) VSM terminal voltage, (d) voltage at PCC, (e) modulation index variation following the 0.1 pu of constant L load addition

The strict control on tracking the set *Q-v* droop characteristic can be seen in synchronverter as well. The integral time constant of the *Q-v* control loop can be controlled to achieve faster

voltage responses, but attention must be given to avoid unnecessary overshoots in the voltage following any disturbance. Synchronverter has been modified to achieve the set active power and reactive power targets in grid-connected mode by removing the paths used for droop action [28].

The responses of synchronverter to a solid three-phase-to-ground fault are given in Figure 4.27. Synchronverter has also resulted in a fault current level of 4.3 pu, which is comparable to other VSM algorithms. The peak rotational speed following the fault is 1.0018 pu, which is closer to the VC-VSC model.

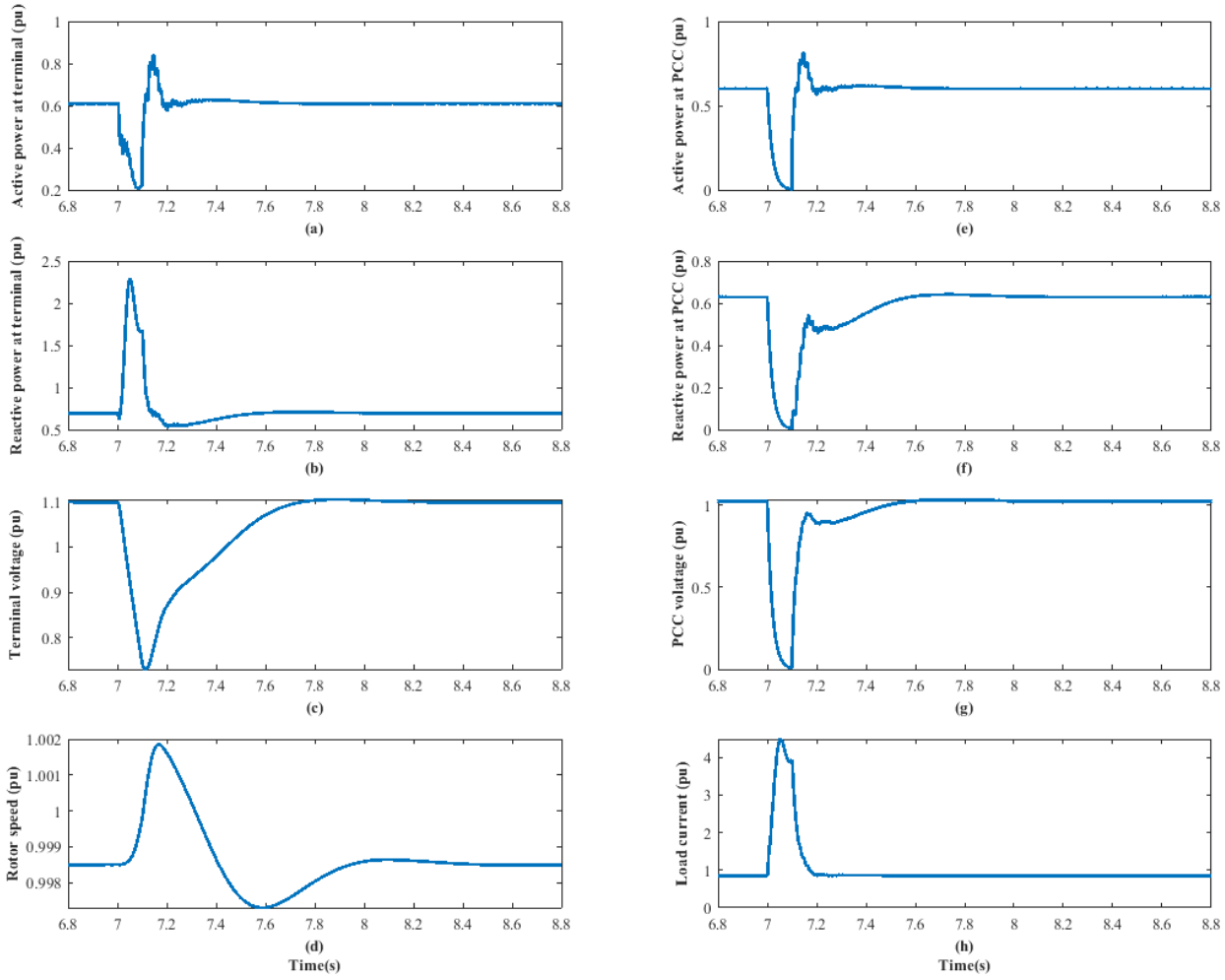

Figure 4.27 Synchronverter model's (a) active power at VSM terminal, (b) reactive power at VSM terminal, (c) VSM terminal voltage, (d) VSM virtual rotor speed, (e) active power at PCC, (f) reactive power at PCC, (g) voltage at PCC, (h) load current variation for a three phase-ground soild fault at PCC for 0.1 s

A HIF, which creates a 0.5 pu voltage reduction at the PCC, is applied to synchronverter model, and the obtained results are given in Figure 4.28. A fault reactance of 0.15 H and the fault duration of 0.1 s are used. The responses are comparable to other VSM algorithms and can be explained similarly.

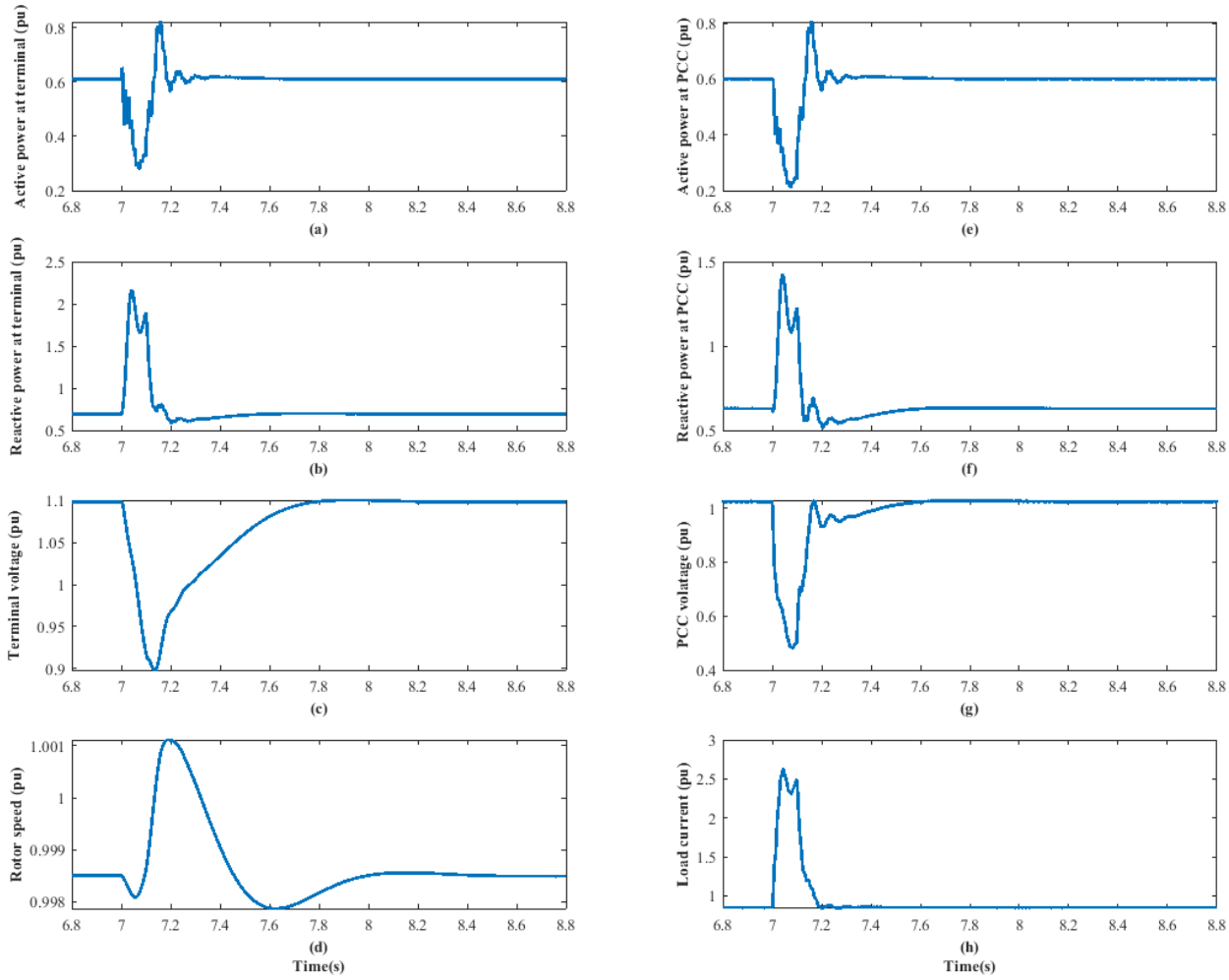

Figure 4.28 Synchronverter model's (a) active power at VSM terminal, (b) reactive power at VSM terminal, (c) VSM terminal voltage, (d) VSM virtual rotor speed, (e) active power at PCC, (f) reactive power at PCC, (g) voltage at PCC, (h) load current variation for three pahse-ground high impedance fault at PCC for 0.1 s

Chapter 5 : Contributions, Conclusions and Recommendations for Future Work

This chapter presents the contributions and conclusions of the study. The suggested future works complete the chapter.

5.1 Contributions

The contributions of this thesis are as follows:

- A number of VSM algorithms were identified and categorized in a simple way, which can be applied generally for every VSM algorithm.
- A detailed switching model in PSCAD/EMTDC was developed to test the grid-forming ability of VSM algorithms with a properly tunned LCL filter.
- A detailed comparative analysis was completed between a conventional SM and the selected VSM algorithms to emphasis on the impacts of VSM controller parameters on its frequency response.
- The following publication resulted from the study. This compares dynamic responses among selected VSM algorithms.

  T. Thilekha, S. Filizadeh, U.D. Annakkage, and C. Karawita, "Comparison of Dynamic Characteristics of Virtual Synchronous Machine Control Algorithms," in *Proc. 2020 CIGRE Canada Conference*, Toronto, ON, Canada, Oct. 2020.

5.2 Conclusions

The conclusions of this thesis are as follows:

- The level of emulated SM characteristics is different for each tested VSM topology. However, their dynamic responses for the same set of large signal disturbances have a closer relationship irrespective of the used SM model.
- LCL filter could successfully suppress the harmonics generated by the two-level voltage source converter for all the tested VSM algorithms.

- The analysis on VSM topologies reveals that f-droop function is a fundamental feature that any VSM topology might present. This ensures output power modulation according to grid frequency regardless of the inertial control action presence.
- The controller parameters including inertia time constant and damping co-efficient can be selected arbitrary. However, those values should be selected subjected to the system load characteristics, allowable bandwidths of controllers, IGBT current ratings, and grid codes.
- VSM0H model provides the fastest frequency response compared to other tested VSM algorithms. Its frequency nadir can be improved by introducing some inertial characteristics via its low pass filter.
- The optimal VSM algorithm for an application can be selected subjected to the required transient response specifications. The proper tunning of VSM control parameters lead to achieve better frequency response.
- The absence the current controlling capability of the tested VSM algorithms has resulted in a larger fault current beyond the converter capability. Therefore, an implementation of the current limiting action is needed.
- All the tests have been carried out using an ideal dc voltage source. The dc side dynamics will also have an impact of VSM operation and need to be fully investigated.

5.3 Future Work

- Incorporation of a current controller to the selected VSM algorithms.
- The dc side dynamics can be adopted to get the full picture of the VSM algorithm's performance.
- Use of ESS on the dc side to assist the VSM to modulate real power exchange with the network may enhanced the overall dynamic response of the converter.

References

[1] “Renewable Energy.” [Online]. Available: https://www.c2es.org/content/renewable-energy/.

[2] “Renewables.” IEA, 2020, [Online]. Available: https://www.iea.org/.

[3] A. Ipakchi and F. Albuyeh, “Grid of the future,” *IEEE Power Energy Mag.*, vol. 7, no. 2, pp. 52–62, Mar. 2009, doi: 10.1109/MPE.2008.931384.

[4] Q.-C. Zhong, “Virtual Synchronous Machines: A unified interface for grid integration,” *IEEE Power Electron. Mag.*, vol. 3, no. 4, pp. 18–27, Dec. 2016, doi: 10.1109/MPEL.2016.2614906.

[5] J. Zhu, C. D. Booth, G. P. Adam, A. J. Roscoe, and C. G. Bright, “Inertia Emulation Control Strategy for VSC-HVDC Transmission Systems,” *IEEE Trans. Power Syst.*, vol. 28, no. 2, pp. 1277–1287, May 2013, doi: 10.1109/TPWRS.2012.2213101.

[6] A. Luna, U. Tamrakar, T. M. Hansen, and R. Tonkoski, “Frequency Response in Grids with High Penetration of Renewable Energy Sources,” in *2018 North American Power Symposium (NAPS)*, Fargo, ND, Sep. 2018, pp. 1–5, doi: 10.1109/NAPS.2018.8600620.

[7] J. Rocabert, A. Luna, F. Blaabjerg, and P. Rodríguez, “Control of Power Converters in AC Microgrids,” *IEEE Trans. Power Electron.*, vol. 27, no. 11, pp. 4734–4749, Nov. 2012, doi: 10.1109/TPEL.2012.2199334.

[8] P. Kundur, *Power System Stability and Control*. New York: McGraw Hill, 1994.

[9] J. Palermo, “International review of frequency control adaptation,” *Aust. Energy Mark. Oper.*, p. 179, Oct. 2016.

[10] J. Fang, H. Li, Y. Tang, and F. Blaabjerg, “On the Inertia of Future More-Electronics Power Systems,” *IEEE J. Emerg. Sel. Top. Power Electron.*, vol. 7, no. 4, pp. 2130–2146, Dec. 2019, doi: 10.1109/JESTPE.2018.2877766.

[11] I. Serban and C. Marinescu, “Control Strategy of Three-Phase Battery Energy Storage Systems for Frequency Support in Microgrids and with Uninterrupted Supply of Local Loads,” *IEEE Trans. Power Electron.*, vol. 29, no. 9, pp. 5010–5020, Sep. 2014, doi: 10.1109/TPEL.2013.2283298.

[12] B. W. Tuinema *et al.*, “Modelling of large-sized electrolysers for real-time simulation and study of the possibility of frequency support by electrolysers,” *IET Gener. Transm. Distrib.*, vol. 14, no. 10, pp. 1985–1992, May 2020, doi: 10.1049/iet-gtd.2019.1364.

[13] S. D’Arco and J. A. Suul, “Virtual synchronous machines-Classification of implementations and analysis of equivalence to droop controllers for microgrids,” in *2013 IEEE Grenoble Conference*, Grenoble, France, Jun. 2013, pp. 1–7, doi: 10.1109/PTC.2013.6652456.

[14] H. Bevrani, T. Ise, and Y. Miura, “Virtual synchronous generators: A survey and new perspectives,” *Int. J. Electr. Power Energy Syst.*, vol. 54, pp. 244–254, Jan. 2014, doi: 10.1016/j.ijepes.2013.07.009.

[15] H. Alrajhi Alsiraji and R. El-Shatshat, “Comprehensive assessment of virtual synchronous machine based voltage source converter controllers,” *IET Gener. Transm. Distrib.*, vol. 11, no. 7, pp. 1762–1769, May 2017, doi: 10.1049/iet-gtd.2016.1423.

[16] S. D’Arco, J. A. Suul, and O. B. Fosso, “A Virtual Synchronous Machine implementation for distributed control of power converters in SmartGrids,” *Electr. Power Syst. Res.*, vol. 122, pp. 180–197, May 2015, doi: 10.1016/j.epsr.2015.01.001.

[17] D. Arricibita, P. Sanchis, and L. Marroyo, “Virtual synchronous generators classification and common trends,” in *IECON 2016 - 42nd Annual Conference of the IEEE Industrial Electronics Society*, Florence, Italy, Oct. 2016, pp. 2433–2438, doi: 10.1109/IECON.2016.7793025.

[18] U. Tamrakar, D. Shrestha, M. Maharjan, B. Bhattarai, T. Hansen, and R. Tonkoski, “Virtual Inertia: Current Trends and Future Directions,” *Appl. Sci.*, vol. 7, no. 7, p. 654, Jun. 2017, doi: 10.3390/app7070654.

[19] S. D’Arco and J. A. Suul, “Equivalence of Virtual Synchronous Machines and Frequency-Droops for Converter-Based MicroGrids,” *IEEE Trans. Smart Grid*, vol. 5, no. 1, pp. 394–395, Jan. 2014, doi: 10.1109/TSG.2013.2288000.

[20] M. Yu *et al.*, “Use of an inertia-less Virtual Synchronous Machine within future power networks with high penetrations of converters,” in *2016 Power Systems Computation Conference (PSCC)*, Genoa, Italy, Jun. 2016, pp. 1–7, doi: 10.1109/PSCC.2016.7540926.

[21] T. Shintai, Y. Miura, and T. Ise, “Oscillation Damping of a Distributed Generator Using a Virtual Synchronous Generator,” *IEEE Trans. Power Deliv.*, vol. 29, no. 2, pp. 668–676, Apr. 2014, doi: 10.1109/TPWRD.2013.2281359.

[22] K. Sakimoto, Y. Miura, and T. Ise, “Stabilization of a power system with a distributed generator by a Virtual Synchronous Generator function,” in *8th International Conference on Power Electronics - ECCE Asia*, Jeju, Korea (South), May 2011, pp. 1498–1505, doi: 10.1109/ICPE.2011.5944492.

[23] M. Guan, W. Pan, J. Zhang, Q. Hao, J. Cheng, and X. Zheng, “Synchronous Generator Emulation Control Strategy for Voltage Source Converter (VSC) Stations,” *IEEE Trans. Power Syst.*, vol. 30, no. 6, pp. 3093–3101, Nov. 2015, doi: 10.1109/TPWRS.2014.2384498.

[24] Y. Hirase, K. Abe, K. Sugimoto, and Y. Shindo, “A grid-connected inverter with virtual synchronous generator model of algebraic type,” *Electr. Eng. Jpn.*, vol. 184, no. 4, pp. 10–21, Sep. 2013, doi: 10.1002/eej.22428.

[25] M. P. N. van Wesenbeeck, S. W. H. de Haan, P. Varela, and K. Visscher, “Grid tied converter with virtual kinetic storage,” in *2009 IEEE Bucharest PowerTech*, Bucharest, Jun. 2009, pp. 1–7, doi: 10.1109/PTC.2009.5282048.

[26] V. Karapanos and Z. Yuan, “A Control Algorithm for the Coordination of Multiple Virtual Synchronous Generator Units,” p. 9.

[27] Q.-C. Zhong and G. Weiss, “Synchronverters: Inverters That Mimic Synchronous Generators,” *IEEE Trans. Ind. Electron.*, vol. 58, no. 4, pp. 1259–1267, Apr. 2011, doi: 10.1109/TIE.2010.2048839.

[28] Qing-Chang Zhong, Phi-Long Nguyen, Zhenyu Ma, and Wanxing Sheng, “Self-Synchronized Synchronverters: Inverters Without a Dedicated Synchronization Unit,” *IEEE Trans. Power Electron.*, vol. 29, no. 2, pp. 617–630, Feb. 2014, doi: 10.1109/TPEL.2013.2258684.

[29] R. Hesse, D. Turschner, and H.-P. Beck, “Micro grid stabilization using the virtual synchronous machine (VISMA),” *Renew. Energy Power Qual. J.*, vol. 1, no. 07, pp. 676–681, Apr. 2009, doi: 10.24084/repqj07.472.

[30] Y. Chen, R. Hesse, D. Turschner, and H.-P. Beck, “Comparison of methods for implementing virtual synchronous machine on inverters,” *Renew. Energy Power Qual. J.*, pp. 734–739, Apr. 2012, doi: 10.24084/repqj10.453.

[31] C. Sun, S. Q. Ali, G. Joos, and F. Bouffard, “Virtual Synchronous Machine Control for Low-Inertia Power System Considering Energy Storage Limitation,” in *2019 IEEE Energy Conversion Congress and Exposition (ECCE)*, Baltimore, MD, USA, Sep. 2019, pp. 6021–6028, doi: 10.1109/ECCE.2019.8913169.

[32] M. A. Swidan, “Study of damping power in interconnected power systems,” 1964.

[33] A. J. Roscoe, M. Yu, A. Dyśko, C. Booth, R. Ierna, and J. Zhu, “A VSM (Virtual Synchronous Machine) Convertor Control Model Suitable for RMS Studies for Resolving System Operator / Owner Challenges,” p. 8.

[34] A. J. Roscoe and S. M. Blair, “Choice and properties of adaptive and tunable digital boxcar (moving average) filters for power systems and other signal processing applications,” in *2016 IEEE International Workshop on Applied Measurements for Power Systems (AMPS)*, Aachen, Germany, Sep. 2016, pp. 1–6, doi: 10.1109/AMPS.2016.7602853.

[35] Fang Gao and M. R. Iravani, “A Control Strategy for a Distributed Generation Unit in Grid-Connected and Autonomous Modes of Operation,” *IEEE Trans. Power Deliv.*, vol. 23, no. 2, pp. 850–859, Apr. 2008, doi: 10.1109/TPWRD.2007.915950.

[36] A. Muthusamy, “Selection of Dynamic performance Control Parameters for Classic HVDC in PSS/E,” Chalmers University of Technology, Sweden, 2010.

[37] K. H. Ahmed, S. J. Finney, and B. W. Williams, “Passive Filter Design for Three-Phase Inverter Interfacing in Distributed Generation,” in *2007 Compatibility in Power Electronics*, Gdansk, Poland, May 2007, pp. 1–9, doi: 10.1109/CPE.2007.4296511.

[38] M. Liserre, F. Blaabjerg, and S. Hansen, “Design and Control of an LCL-Filter-Based Three-Phase Active Rectifier,” *IEEE Trans. Ind. Appl.*, vol. 41, no. 5, pp. 1281–1291, Sep. 2005, doi: 10.1109/TIA.2005.853373.

[39] M. Said-Romdhane, M. Naouar, I. Belkhodja, and E. Monmasson, “An Improved LCL Filter Design in Order to Ensure Stability without Damping and Despite Large Grid Impedance Variations,” *Energies*, vol. 10, no. 3, p. 336, Mar. 2017, doi: 10.3390/en10030336.

[40] H. N. Villegas, “Electromechanical Oscillations in Hydro-Dominant Power Systems: An Application to the Colombian Power System,” Master of Science, Iowa State University, Digital Repository, Ames, 2011.

[41] Conseil international des grands réseaux électriques and Comité d’études B5, *High impedance faults*. Paris: CIGRÉ, 2009.